This is a post-peer-review, pre-copyedit version of an article published in Earth-Science Reviews. The final authenticated version is available online at: https://doi.org/10.1016/j.earscirev.2019.102958

Seafloor massive sulfides from mid-ocean ridges: Exploring the causes of their geochemical variability with multivariate analysis

Luca Toffolo[1], Paolo Nimis[1], Gennady A. Tret'yakov[2], Irina Y. Melekestseva[2], Victor E. Beltenev[3]

[1] Dipartimento di Geoscienze, Università degli Studi di Padova, Via Gradenigo 6, 35131 Padova, Italy.

[2] South Urals Federal Research Center, Urals Branch of Russian Academy of Sciences, Institute of Mineralogy, Miass, Chelyabinsk District, 456317 Russia.

[3] Polar Marine Geosurvey Expedition, Pobedy st. 24, Lomonosov–St. Petersburg, 198412 Russia.

Corresponding author: Paolo Nimis (paolo.nimis@unipd.it)

Declarations of interest: none

Highlights:

- The geochemical variability of massive sulfides from mid-ocean ridges is explored with multivariate statistical analysis.
- The observed variability is mostly related to the temperature of deposition, the ridge spreading rate and zone refining.

- The nature of the substrate (mafic vs. ultramafic rocks) seems to play a secondary role in controlling metal associations.

Abstract

The neovolcanic zones of mid-ocean ridges are host to seawater-derived hydrothermal systems forming seafloor massive sulfide (SMS) deposits. These deposits have high concentrations of base metals and potentially economic enrichment of a wide range of trace elements. The factors controlling this enrichment are currently poorly understood. We have investigated the main factors controlling SMS compositional variability through robust principal component analysis and robust factor analysis of published and newly obtained bulk geochemical data for samples collected from SMS deposits worldwide. We found that a large part of the observed variability is produced by a combination of three independent factors, which are interpreted to reflect (in order of importance): (1) the temperature of deposition, (2) the ridge spreading rate, and (3) zone refining. The first and the third factors are mostly related to processes operating near the seafloor, such as conductive cooling, mixing of the hydrothermal fluids with seawater and metal remobilization, and determine the relative proportions of the main minerals and, thus, of Cu and Zn (Co, Se, Sb, Pb). The ridge spreading rate influences the structure of the oceanic lithosphere, which exerts a major control on the length and depth of the hydrothermal convection cell and on the rock-to-water ratios in the reaction zone, which in turn control the behavior of the precious metals Au and Ag and elements including Ni (Mo, Se). Despite the obvious role of substrate rocks as metal sources, their composition (specifically mafic vs. ultramafic) does not emerge as a statistically significant independent factor.

Keywords: seafloor massive sulfides, mid-ocean ridges, geochemistry, multivariate analysis

1 Introduction

Seafloor massive sulfides (SMS) are stratiform or stratabound accumulations of base metal sulfides that formed on or near the seafloor by precipitation from dominantly seawater-derived hydrothermal fluids (Hannington, 2014). Since their discovery in 1978 at the East Pacific Rise (Francheteau et al., 1979), SMS deposits have been recognized along many neovolcanic plate boundaries, including mid-ocean ridges, submarine arc volcanoes and back-arc spreading centers. In all these environments, magma intrusions sustain hydrothermal convective cells, in which percolating seawater leaches metals from the substrate rocks (Sleep, 1983; Tivey, 2007). Upon ascent, metals precipitate primarily as sulfides below and on the seafloor, as the hot (up to ~400 °C) and acidic (pH at 25 °C as low as ~3) hydrothermal fluid quenches in the presence of cold (~2 °C) and alkaline (pH at 25 °C ~ 8) seawater. Considering the total length of neovolcanic plate boundaries, SMS deposits could represent a significant source of metals, estimated at $\sim 3 \times 10^7$ tonnes of Cu + Zn (Hannington et al., 2011). Moreover, some deposits have remarkable grades of gold and silver (up to several tens of ppm; Petersen and Hein, 2013). Unraveling the factors that affect the geochemistry of SMS is important to the understanding of their genesis and for developing effective guidelines for the exploration and economic evaluation of both present-day seafloor deposits and their ancient on-land analogues.

Observations on SMS deposits show that the geochemistry of the massive sulfides is primarily related to the geodynamic setting in which they are formed. On mid-ocean ridges, where the hydrothermal fluids dominantly leach mafic or ultramafic substrates, SMS typically have high concentrations of Cu + Zn (>> Pb) (Hannington et al., 2005). The leaching of elements from substrate rocks is influenced by the structure of the oceanic lithosphere and by the nature of the hydrothermal convection, which are essentially related to the spreading rate (Bougault et al.,

1993; Bach and Humphris, 1999; Coumou et al., 2009). On *slow-spreading* ridges, for instance, the magma supply is low and part of the extension is accommodated by deep-rooted detachment faults. Therefore, the lithosphere is not layered and is mainly composed of gabbros and ultramafic rocks (MacLeod et al., 2009; Lowell, 2010). In this setting, low heat fluxes and deep-rooted faults favor long and deep fluid pathways, which enhance fluid-rock interaction at relatively high rock-to-water (r/w) ratios (Bach and Humphris, 1999). By contrast, on *fast-spreading* ridges, the magma supply is high, the lithosphere is typically layered and the upper basaltic section is highly permeable (Coumou et al., 2008). The resulting higher heat flux, together with episodic diking events, favor the development of shallower and ephemeral hydrothermal convection cells (Wilcock and Delaney, 1996). Therefore, fast-spreading ridges are typified by less evolved seawater-dominated fluids (i.e., lower r/w ratios). Irrespective of spreading rate, SMS deposits show significant geochemical variability along the same ridge and even at the deposit or hand-specimen scale (Petersen and Hein, 2013), suggesting a complex interplay of regional and local controls. In fact, some specific geochemical features (e.g., Au enrichment and Au/Ag and Co/Ni ratios) have been variably related to the nature of the substrate (e.g., mafic vs. ultramafic rocks), phase separation processes in the fluid, the presence of a magmatic influx of volatiles and metals, the morphology of vent structures (tubular vs. beehive chimneys generated by focused or diffuse fluid flow, respectively), the ridge spreading rate, or a combination of these factors (Marques et al., 2006; Fouquet et al., 2010; German et al., 2016; Melekestseva et al., 2017; Knight et al., 2018). However, the relative role of these factors in controlling the geochemical variability of SMS deposits is still poorly defined. Part of this uncertainty is due the fact that the nature of the substrate is inferred from two-dimensional seafloor observations and different lithologies may occur in the areas surrounding the deposits.

Also, individual deposits may show a mixture of apparent geochemical signatures (e.g., 'mafic' and 'ultramafic'; Marques et al., 2006; Webber et al., 2015; Melekestseva et al., 2017). Moreover, experimental works on rock/seawater interactions under conditions typical of subseafloor reaction zones so far mainly explored the behavior of only a few base metals (Fe, Mn, Zn, Cu, Ni) in basalt-seawater systems at r/w ratios ranging from ~0.001 to 2 (Seyfried and Bischoff, 1977, 1981; Seyfried and Mottl, 1982; Seyfried and Janecky, 1985; Seewald and Seyfried, 1990). Experiments on peridotite-seawater systems investigated even fewer base metals (Fe, Mn, Ni, Zn) and only at r/w < 0.1 and T ≤ 300 °C (Seyfried and Dibble, 1980; Janecky and Seyfried, 1986). Forward thermodynamic modeling of rock-seawater reactions and hydrothermal fluid cooling has been used to investigate the behavior of a larger number of elements in seafloor hydrothermal systems (Janecky and Seyfried, 1984; McCollom and Shock, 1998; Wetzel and Shock, 2000; Palandri and Reed, 2004; Klein et al., 2013; Melekestseva et al., 2014, 2017; Fuchs et al., 2019). However, the resulting models are specific to particular rock compositions reacting under fixed conditions or to particular fluid compositions and are not generally applicable to all hydrothermal systems on mid-ocean ridges.

In this work, we investigate the first-order controls on the compositions of SMS deposits on mid-ocean ridges by means of multivariate statistical analysis of published and novel bulk chemical analyses of SMS samples from seafloor hydrothermal fields worldwide. Attempts to apply multivariate statistical analysis to SMS at various scales were previously made by Hannington et al. (1991a) and Fouquet et al. (2010). Hannington et al. (1991a) applied factor analysis to mafic-hosted deposits worldwide and found important geochemical associations for Sb-Pb-Au-Ag and Mo-Co-Se-Cu-Fe, reflecting metal associations of low- and high-temperature mineral assemblages, respectively. Fouquet et al. (2010) used principal component analysis to

identify site-specific geochemical groups (i.e., Cu-rich high-temperature, Zn-rich intermediate-temperature, and oxide/sulfate, respectively) in ultramafic-hosted deposits at the Mid-Atlantic Ridge. Compared with these previous works, the dataset considered here is more comprehensive as it is built on four times the sample number analyzed by Hannington et al. (1991a), covers more ridges and includes data from both mafic- and ultramafic-hosted SMS deposits. Moreover, in this work we use robust principal component analysis (rPCA) and robust factor analysis (rFA) to limit the influence of noise from individual anomalous samples. This is particularly useful, because analyzed SMS materials mostly consist of dredged samples and are certainly affected by sampling bias (Fuchs et al., 2019). Therefore, our analysis provides a better assessment of the first-order factors that control the geochemical variability of ridge-hosted SMS at a global scale. By comparing the results with existing experimental data and new thermodynamic models, we show that temperature of deposition, seafloor spreading rate and r/w ratio, and zone refining are the major factors controlling metal associations in SMS deposits and that, contrary to common belief, the nature of the substrate may be of secondary importance.

2 Materials and Methods

Based on an initial database by Hannington et al. (2004), we have compiled published and unpublished bulk chemical analyses of sulfides samples collected from SMS deposits located on mid-ocean ridges. New analyses of samples from the Irinovskoe, Krasnov and Peterburgskoe SMS fields at the Mid-Atlantic Ridge (Table 1) were acquired at the South Urals Federal Research Center, Urals Branch of Russian Academy of Sciences, Institute of Mineralogy (Miass, Russia) using atomic absorption (AA) analysis in air-acetylene flame on a Perkin Elmer 3110 spectrometer (Co, Ni, Cu, Zn, Pb, Au, Ag) and inductively coupled plasma-mass spectrometry (ICP MS) on an Agilent 7700x mass spectrometer (Sb, Se, Mo). For AA analyses of Co, Ni, Cu,

Zn and Pb, 0.5–1.0 g of sample material was dissolved in a 15-ml mixture of HF, HCl, and HNO_3, heated first up to 100–150°C and then to 250°C, and concentrated to the formation of wet salts. This procedure was conducted three times, then the samples were dried, cooled, mixed with 3 ml concentrated HNO_3, and filtered. For AA analyses of Au and Ag, 1 g of sample material was diluted in a mixture of 30 ml HCl and 10 ml HNO_3, concentrated on the oven to the formation of wet salts, filtered using HCl solution and cooled. For ICP-MS analyses, the sample material was initially digested in Teflon autoclaves using a mixture of HF, HCl and HNO_3 in a SpeedWave microwave digestion system (Berghof, Germany) using a two-stage heating procedure to a temperature of up to 180°C for 40 minutes. After digestion, the fluorine complexes were decomposed by double evaporation of the dry residual with concentrated HNO_3 at 110°C in glassy carbon crucibles. The precipitates were further dissolved in hot 0.5 N HNO_3 and subsequently reduced to a 100-ml aliquot. All pure acids used for digestion were purified in a BSB-939-IR apparatus (Berghof, Germany). The water for dilution was deionized in a Milli-Q® Integral Water Purification System by Millipore, US. Quality control of the analytical procedure was performed by analysis of state reference materials (GSO) of water metal solutions (7256-96 Zn, 7252-96 Pb, 7265-96 Ni, 7268-96 Co, 7255-96 Cu, and 8402-2002 Ag) and flotation concentrate of Au-bearing ore CZK-3 (2739-83 Au) for AA analysis. Indium was used as an internal standard calibrated against the USGS BCR-2 rock reference material for ICP MS analyses.

For the statistical analysis, we only considered reportedly fresh SMS samples representing fragments of hydrothermal chimneys and mounds. We excluded samples which contained significant proportions of weathering products or silicate gangue (e.g., Al_2O_3 and MgO contents > 2 wt.%). The presence of silica phases, which do not typically contain significant

161 trace elements, was not considered critical. Since the chemical analyses were heterogeneous in
162 terms of analyzed elements and their detections limits, we only selected those records that
163 provided data for a sufficiently large number of elements (i.e., Au, Ag, Co, Mo, Ni, Sb, Se, Cu,
164 Zn, Pb). Barite-rich (Ba > 1 wt.%) samples were excluded to avoid possible bias caused by
165 elements (Pb, Co, Ni, Sb) incorporated in or adsorbed on barite (cf. Melekeststeva et al., 2014;
166 Safina et al., 2016). Analyses reported only as averages of several samples were discarded, since
167 these data were not accompanied by adequate mineralogical and textural descriptions of
168 individual samples. These choices allowed us to maintain a balance between the number of
169 elements (N = 10), the number of records (N = 426) and the number of represented hydrothermal
170 sites or clusters (N = 26; Table 2). For instance, due to the incompleteness of many published
171 analyses, adding a single element such as As would have decreased the number of represented
172 sites to 25 (the Beebe hydrothermal field would be completely excluded). The SMS deposits
173 were grouped on the basis of the ridge spreading rate [fast, intermediate, and (ultra)slow] and
174 host-rock composition (mafic or ultramafic). The complete database (Table S1) includes samples
175 from 3 sites on fast, 8 sites on intermediate, 12 sites on slow, and 3 sites on ultraslow spreading
176 ridges (Table 2). The distinction between mafic-hosted and ultramafic-hosted deposits was not
177 always straightforward, because both types of rocks generally occur in the areas surrounding and
178 probably beneath nominally ultramafic-hosted deposits. In this work, deposits classified as
179 ultramafic-hosted ($N_{ultramafic}$ = 6 out of a total of 26) are those sited on substrates that, based on
180 reported geological evidence, are likely to contain abundant ultramafic rocks (Table 2). The

resulting mafic-hosted vs. ultramafic-hosted classification is the same as that used in the recent review by Fuchs et al. (2019).

The statistical relationships between elements were explored by using both non-parametric and parametric techniques for dimension reduction, i.e., rPCA and rFA, respectively. The former technique has the advantage of not being influenced by the user's decisions and is, therefore, more appropriate at an exploratory stage. The latter technique is dependent on the number of chosen factors, but, unlike rPCA, it does not force the factors to explain all the variability (Reimann et al., 2008). Therefore, rFA may be more effective in defining statistical factors that are representative of common geochemical processes (Reimann et al., 2002). Accordingly, we used rPCA to guide rFA, in the sense that the number of principal components that explained most of the variability in rPCA were used to determine the proper number of factors for rFA (Reimann et al., 2008). The statistical analyses were performed with the R software using the function "pcaCoDa" in the "robCompositions" library (Templ et al., 2011) and the R script (principal factor analysis with a varimax rotation) by Filzmoser et al. (2009a). Robust methods were preferred to "classical" methods, because they are less sensitive to outliers (Filzmoser et al., 2009b; Filzmoser and Hron, 2011), which are common in geochemical data. Isometric logratio and centered logratio transformations were applied to the data used for rPCA and rFA, respectively. These transformations have the advantage of opening the data, but require that no zeros are present in the data matrix. Therefore, we represented concentrations below the detection limit by multiplying the detection limit by 0.65. This choice is statistically appropriate

since only 5.3% of the data are below detection limit (Palarea-Albaladejo and Martín-Fernández, 2015; Martín-Fernández et al., 2003).

To obtain independent constraints for the interpretation of the statistical data, we simulated the basalt–seawater and peridotite–seawater reactions in a model subseafloor hydrothermal reaction zone. Thermodynamic calculations were performed by Gibbs energy minimization using the Selektor program (Karpov et al., 1997; Chudnenko, 2010). Rock–seawater reactions were modeled at 400°C and 30 MPa assuming various r/w ratios. Complete details on the modeling procedure and the choice of thermodynamic data are reported in Melekestseva et al. (2017). The compositions of basaltic glass and peridotite were taken from Lehnert et al. (2000) and Fouquet et al. (2010), respectively. Molybdenum content in basalt (0.31 ppm) and seawater (1.04×10^{-7} mol/kg H_2O) were taken from Fouquet et al. (2010) and Steele et al. (2010), respectively. Seawater and reactant rock compositions are reported in Table S2.

3 Results

3.1 Element distribution

The distribution of elements in mid-ocean ridge SMS is reported in Table 2 and illustrated by box-and-whiskers plots in Fig. 1. Median element concentrations include ~3 wt.% Cu, ~1 wt.% Zn, ~0.02 wt.% Pb, ~270 ppb Au, ~110 ppm Co, ~60 ppm Se, ~50 ppm Mo, ~20 ppm Ag, ~10 ppm Ni, and ~5 ppm Sb.

3.2 Robust PCA and FA

The rPCA was used to determine the number of factors suitable to describe the compositional variability of the SMS deposits. The results of the rPCA are illustrated in

the scree plot in Fig. 2 (see Fig. S1 for complete score plot). The line connecting the eigenvalues shows a progressive decrease in slope from PC1 to PC4 and only minor changes beyond PC3. Moreover, the first three components together explain most of the variability (~75%). For these reasons, three factors were chosen in the subsequent factorial analysis. As shown in Fig. 3, the most important variables in the first factor (F1) are Pb and Sb (plus minor contributions by Zn and Ag) with positive loadings and Cu and Se (Co) with negative loadings. The second factor (F2) is mainly related to Au and Ag (negative loadings) and more weakly affected by Mo, Se and Ni (positive loadings). The third factor (F3) is mostly influenced by Zn (Sb, Ag) (positive loadings) and Co (Mo) (negative loadings). The score plots in Fig. 4 show the distribution of the samples in the space defined by the factors. Figure S2 shows the same results for individual sites. The samples are scattered through the plots, which indicates that rFA was effective in detecting the directions of maximum variability. Most remarkably, the F1 vs. F2 plot (Fig. 4A) shows that the factor F2 [Se-Mo-Ni vs. Au-Ag] discriminates well between SMS samples from slow-spreading ridges (Mid-Atlantic Ridge, Mid-Cayman Rise, Central Indian Ridge) and those from intermediate/fast-spreading ridges (Southern Explorer Ridge, Juan de Fuca Ridge and Galapagos Rift). The great majority (87%) of the samples from intermediate/fast-spreading ridges show positive F2 loadings and only 7% of them show F2 loadings <–0.1. Most of these low-F2 samples are from the sedimented, intermediate-spreading Gorda Ridge (Escanaba Trough) and Juan de Fuca Ridge (Middle Valley) (Fig. S2A). The great majority (84%) of the samples from slow-spreading ridges show negative F2 values and only 4% of them show F2 values >+0.1. No particular cluster is apparent in the F1 vs. F3 plot (Fig. 4B), although all but one

samples from the Escanaba Trough and all samples from the mafic-hosted Petersbursgkoe field of the slow-spreading Mid Atlantic Ridge show more or less negative F3 scores (Fig. 4B and Fig. S2B). The F2 vs. F3 plot (Fig. S3) does not show any additional remarkable features and only confirms the good discrimination between SMS from intermediate/fast- and slow-spreading ridges. Concerning samples from slow-spreading ridges (low F2), the ultramafic-hosted SMS have, on average, lower values of F1 relative to the mafic-hosted SMS (Fig. 4A). Nonetheless, the ranges of factors F1, F2 and F3 covered by the two groups of samples are similar and no clear distinction between mafic- and ultramafic-hosted deposits is apparent in either plots (Fig. 4A,B). Since the ultramafic-hosted deposits are undersampled in our database ($N_{ultramafic}$ = 64; N_{mafic} = 362), it may be argued that these results are biased due to the disproportionate weight of the mafic-hosted deposits. To test this possibility, we have performed rFA on a reduced data set in which the mafic records were randomly selected to match the number of the ultramafic records (Fig. S4). The resulting statistical factors F1 and F2 are very similar in terms of both element associations and relative factor weights to those obtained using the complete database (cf. Fig. 4). The discrimination between fast/intermediate-spreading and slow-spreading ridges is somewhat less effective, probably due to the smaller number of input data, but there is still substantial overlap between ultramafic-hosted and mafic-hosted deposits from slow-spreading ridges. This confirms the robustness of our rFA analysis.

3.3 Thermodynamic modeling

The complete results of thermodynamic modelling of basalt/seawater and peridotite/seawater reactions at 400°C, 30 MPa, and log(r/w) ratios ranging between –5

and 0 are shown in Fig. S5 and Fig. S6. The most relevant results are summarized in Fig. 5. The first consequence of basalt/seawater and peridotite/seawater reactions is the development of alteration mineral assemblages, the nature of which in turn affects the composition of the hydrothermal fluid (Fig. S5 and S6).

In the basalt/seawater system, at very low log(r/w) (–5 to –3.1) the secondary mineral assemblage includes chrysotile, Mg chlorite, anhydrite, hematite, and titaniferous oxides, plus brucite at log(r/w) <–3.6 (Fig. 5A). Within this log(r/w) range, the seawater-buffered system is characterized by a high redox potential ($Eh_{400°C}$ ~ 0.2 V). The $pH_{400°C}$ values decrease from ~7.7 at log(r/w) –5 to ~6.3 at log(r/w) –3.1. With increasing log(r/w), the formation of abundant secondary silicates (talc, quartz, amesite, actinolite, Mg-Mn chlorite, epidote, albite) and chromite produces a jump in fluid $pH_{400°C}$ to ~6.7 and then a further progressive increase to ~7.4 at log(r/w) 0. At the same time, $Eh_{400°C}$ drops to –0.4 V at log(r/w) –3 and then further decreases to below –0.6 V (Fig. 5A). At log(r/w) > –1.8 hematite is replaced by magnetite. At log(r/w) > –1.3, when $Eh_{400°C}$ goes below ~ –0.6 V ($\log fO_2$ ~ –25), several sulfides are also formed (Fig. 5A). The computed alteration assemblages are consistent with natural and calculated assemblages in altered oceanic basalts (Alt et al., 1986; McCollom and Shock, 1998; Wetzel and Shock, 2000). Figure 5A shows the calculated concentrations of several elements in the fluid as a function of the r/w ratio. The Fe and, in part, the Si contents are closely related to the Eh and pH values. The chalcophile elements accumulate in the fluid until their respective sulfides are stabilized in the altered rock, and then their concentrations in the fluid decrease. A subsequent minor increase of Co at log(r/w) > –0.3 is related to the disappearance of Co-bearing pyrite. The change in the Ni curve at log(r/w) –2.6 coincides

with a change in the Ni contents of amesite, whereas that at log(r/w) –1.7 is related to the disappearance of Ni-bearing amesite. Formation of Ni-bearing sulfides at log(r/w) –1.2 produces a slight decrease in Ni concentrations to log(r/w) 0. Gold and Ag progressively accumulate in the fluid with increasing r/w ratios.

In the peridotite/seawater system, the secondary mineral assemblage is dominated by chrysotile at all r/w ratios (Fig. S6). At log(r/w) <–4 the seawater-buffered system is characterized by relatively high $Eh_{400°C}$ (~ 0.1 V) and $pH_{400°C}$ (~7.8). With increasing log(r/w), the stabilization of titaniferous oxides is accompanied by a slight decrease in pH to 6.8 at log(r/w) –2.6. With further increasing log(r/w), the pH variations are complicated due to the formation and disappearance of various secondary silicates (chlorite, phlogopite–biotite s.s., talc, actinolite) and show an overall increase, reaching a value of ~7.8 at log(r/w) 0. The $Eh_{400°C}$ values show a nearly flat profile to log(r/w) –3.3, then a marked drop to –0.5 V and a further decrease to below –0.8 V at log(r/w) 0 (Fig. 5B). Hematite is part of the alteration assemblage at log(r/w) <–2.5 and is replaced by magnetite at higher log(r/w). At log(r/w) >–2, when $Eh_{400°C}$ goes below –0.6 V ($\log fO_2$ ~ –25), several sulfides are also formed (Fig. 5B). The computed alteration assemblages are fairly consistent with natural and calculated assemblages in altered oceanic peridotites (Wetzel and Shock, 2000; Palandri and Reed, 2004; Klein and Bach, 2009; Klein et al., 2013). Element contents in the fluid follow broadly similar trends vs log(r/w) as in the basalt/seawater system (Fig. 5). Fe and Si contents are closely related to variations of Eh, pH and silicate mineralogy, Au and Ag progressively accumulate in the fluid, and the concentrations of the chalcophile elements increase until their respective sulfides are formed. The stabilization of (Co, Ni)-bearing sulfides occurs at somewhat lower log(r/w)

than in the basalt/seawater system. The $Eh_{400°C}$ and fO_2 profiles are not strongly dissimilar in the two systems, except at log(r/w) ratios >–0.5, where the peridotite/seawater system becomes more strongly reduced.

4 Discussion

4.1 The effect of temperature

Factor F1, which explains 49% of the variability, is dominated by the anti-correlated groups of elements Cu-Se-(Co) and Pb-Sb-(Zn-Ag) (Fig. 3 and 4). We interpret this anti-correlation to reflect variations in the formation temperature of the mineral assemblages analyzed. Because chalcopyrite solubility in vent fluids drops below 350–375 °C, higher temperature fluids precipitate chalcopyrite-rich (i.e., Cu-rich) assemblages, while lower temperature fluids precipitate Pb-Sb-bearing assemblages with variable proportions of galena and sulfosalts (Janecky and Seyfried, 1984; Seyfried and Ding, 1995). The strong correlation between Se and Cu reflects the ability of Se to replace S in high-temperature chalcopyrite (Huston et al., 1995). Cobalt, which as a divalent cation can substitute for Fe^{2+} and Zn^{2+}, can also be structurally hosted in chalcopyrite, as well as in high-temperature (> 300 °C) Fe-sulfides (Vaughan and Rosso, 2006; Cook et al., 2009; Grant et al., 2018). Galena and sulfosalts are often present only as (sub-)microscopic inclusions in low-temperature assemblages (e.g., Wohlgemuth-Ueberwasser et al., 2015; Grant et al., 2018) and may thus not have been reported in sample descriptions summarized in Table S1. Nonetheless, Grant et al. (2018) showed that significant concentrations of Pb, Ag and Sb in pyrite from relatively cold and distal parts of the TAG sulfide mound were in fact related to inclusions of galena and sulfosalts.

The small positive loading of Zn in factor F1 is consistent with the tendency of sphalerite to precipitate at intermediate to low temperatures (T < ~300 °C; Janecky and Seyfried, 1984). The association of Sb with Pb and Zn may in part reflect substitution of Sb for Pb in galena (Sharp and Buseck, 2003) or for Zn in sphalerite (Maslennikov et al., 2017).

The depositional temperature is mostly controlled by conductive cooling of the hydrothermal fluids or mixing with cold seawater and can vary in time and space at the scales of individual hydrothermal fields (e.g., among different vents or as an effect of waning hydrothermal activity) and even samples (cf. the zonal structure of sulfide chimneys, showing chalcopyrite-rich inner portions formed at higher temperatures and pyrite-sphalerite-rich external portions formed at lower temperatures) (Hannington, 2014). This explains why samples from the same SMS deposit may plot at opposite ends with respect to factor F1 (Fig. S2). The tendency of samples from ultramafic-hosted SMS to show lower F1 loadings than mafic-hosted SMS from the same ridges may reflect the more diffuse high-temperature discharge and, thus, the widespread enrichment in high-temperature elements at the surface of these deposits (Fouquet et al., 2010).

4.2 The influence of ridge spreading rate

Factor F2, which explains 17% of the variability, provides a discrimination between Au-Ag-rich SMS from slow-spreading ridges and Au-Ag-poor, but relatively Ni-Mo-Se-rich, SMS from intermediate/fast-spreading ridges (Fig. 4A). This is in line with the observation by Knight et al. (2018) that the Au content in seafloor SMS is negatively correlated with the ridge spreading rate. Knight et al. (2018) suggested several possible explanations for this geochemical distinction, including the intensity and

duration of fluid-rock interaction, variations in the Au content in the source rocks and differences in fluid chemistry. Here we discuss the possible causes in the light of existing geochemical data and of our statistical analysis and geochemical modeling.

The composition of the substrate has been invoked as an important factor in controlling Au enrichment. However, the absolute average Au concentration in ultramafic rocks (0.49 ppb) is not much higher than that in mid-ocean ridge basalts (MORBs) (0.34 ppb) and is unlikely to determine a significant difference in the amount of Au dissolved in the hydrothermal fluids (Fouquet et al., 2010; Melekestseva et al., 2017; Fuchs et al., 2019). Thus, even assuming a metal contribution from ultramafic rocks for all Au-rich SMS from slow-spreading ridges, the Au content in the substrate alone cannot explain their distinct geochemistry.

In our database, the samples with the lowest F2 scores are those from the ultramafic-hosted Irinovskoe, Kairei, Logatchev 1 and Rainbow sites and from the mafic-hosted Beebe and TAG sites. The fluids venting at Kairei, Logatchev 1 and Rainbow are relatively reduced (Kairei: $\log fO_{2,\,350\,^{\circ}C} \sim -31$ and $H_2 \sim 5$ mM; Logatchev 1: $\log fO_{2,\,350\,^{\circ}C} \sim -32.3$ and $H_2 \sim 12$ mM; Rainbow: $\log fO_{2,\,350\,^{\circ}C} \sim -33.6$ and $H_2 \sim 16$ mM; Charlou et al., 2002; Kumagai et al., 2008; Seyfried et al., 2011; Kawasumi and Chiba, 2017) and similar redox states are expected for fluids from Beebe as they have similar H_2 concentrations ($H_2 \sim 20$ mM; McDermott et al., 2018). Higher fO_2 are reported for TAG vent fluids ($\log fO_{2,\,350\,^{\circ}C} \sim -29$; $H_2 \sim 0.2$ mM; Charlou et al., 1996; Kawasumi and Chiba, 2017), which have a redox state within the range of vent fluids from other mafic-hosted sites on the East Pacific Rise ($\log fO_{2,\,350\,^{\circ}C} \sim -28$ to -29, $H_2 \sim 0.1$ mM, at 13° N; $\log fO_{2,\,350\,^{\circ}C} \sim -29$ to -31, $H_2 \sim 0.4$ mM, at 21° N; Tivey, 1995; Pester et al., 2011; Kawasumi

and Chiba, 2017), Juan de Fuca ($\log f O_{2,\,350\,^{\circ}C} \sim -29$ to –30, $H_2 \sim 0.4$ mM, at Main Endeavour Field; Seewald et al., 2003; Kawasumi and Chiba, 2017) and Central Indian Ridge ($\log f O_{2,\,350\,^{\circ}C} \sim -28$ to –29, $H_2 \sim 0.2$ mM, at Edmond Hydrothermal Field; Gallant and Von Damm, 2006; Kumagai et al., 2008 Kawasumi and Chiba, 2017). Detailed data on fluid chemistry are not available for Irinovskoe. A plot of Au vs. H_2 (Fig. 6) shows that the median Au concentration is generally higher in SMS from slow-spreading ridges and that the highest values are observed at sites where the vent fluids are the most reduced, suggesting a genetic link between Au enrichment and fluid redox state. Note that the number of SMS samples with reported Au concentrations that could be plotted in Figure 6 for the highly variable TAG is much larger than that included in the filtered database used for the multivariate rPCA and rFA (cf. Table 2 and S1), which justifies its relatively low median Au (Fig. 6) in spite of its relatively low F2 scores (Fig. 4). Fluids venting at sites with the highest Au and H_2 contents range from vapor-dominated (e.g., Beebe; McDermott et al., 2018) to seawater- (e.g., Logatchev; Charlou et al., 2002) or brine-dominated (e.g., Kairei and Rainbow; Charlou et al., 2002; Gallant and Von Damm, 2006). The variable chlorinities of fluids vented at sites characterized by similar Au endowment suggest that phase separation is not the primary factor in determining the overall Au enrichment.

The apparent correlation between Au enrichment and redox state must be considered cautiously. In fact, present-day vent fluid compositions may not be fully representative of a specific site, as vent fluid composition can considerably vary in time and space even within the same hydrothermal field (Lowell et al., 1995). This can partially explain why sulfide samples from TAG, for which the most comprehensive

sample set is available, also show the largest compositional variability (Fig. 6). More generally, relations based on absolute element concentrations are unavoidably affected by sampling bias. More robust information can be obtained by considering the geochemical relations of Au with other elements and particularly with those having large positive or negative loadings in factor F2 (i.e., Ni, Mo, Se, and Ag).

In the oceanic lithosphere, Ni, Mo, Se, Au, and Ag are typically stored in sulfides (Patten et al., 2016; Holwell et al., 2017). Therefore, the presence of these elements in seafloor hydrothermal fluids is strictly related to alteration and re-precipitation of sulfides in the substrate rocks. A high temperature in the reaction zone may enhance Au (and H_2) concentrations in the fluid (McDermott et al., 2018), but it would also increase Ni solubility (Liu et al., 2012). Therefore, reaction temperature cannot explain factor F2, in which Au and Ni are anti-correlated (Figs. 3 and 4**)**. Fuchs et al. (2019) showed that, in ultramafic-dominated systems, strongly reduced hydrothermal fluids such as those produced by peridotite serpentinization promote the deposition of Au at relatively high temperatures. This may support a link between fluid redox state and Au endowment (cf. Fig. 6). However, the similar F2 scores shown by mafic- and ultramafic-hosted SMS from slow-spreading ridges (Fig. 4A) suggest that Au enrichment and redox conditions may be largely independent of seafloor substrate composition. Thermodynamic modeling of basalt–seawater and peridotite–seawater reactions shows that, at a given temperature, the concentrations of metals in the fluid are chiefly controlled by r/w ratios and sulfide solubility (Fig. 5). At low r/w ratios, relatively oxidized seawater-dominated fluids favor sulfide dissolution (Palandri and Reed, 2004; Liu et al., 2012; Holwell et al., 2017; Melekestseva et al., 2017). The enrichment in Ni relative to Au and Ag in SMS deposits

427 from intermediate/fast-spreading ridges may thus be an effect of the enhanced dissolution
428 of Ni-rich magmatic sulfides. Higher r/w ratios, which should be more typical of slow-
429 spreading ridges, would instead stabilize sulfides that may segregate Ni while the
430 concentrations of dissolved Au and Ag progressively increase (Fig. 5; see also
431 Melekestseva et al., 2017). High r/w ratios can potentially also be achieved in reaction
432 zones beneath sedimented ridges, where the low-porosity sediment cover may limit
433 seawater fluxes through the oceanic crust. This may explain why most of the samples
434 from the intermediate-spreading, but sedimented, Gorda and Juan de Fuca ridges have
435 low F2 scores similar to samples from slow-spreading ridges (Fig. 4A). Several other
436 elements, which, based on thermodynamic modeling, should also be sensitive to r/w
437 ratios (Fig. 5), do not appear to be controlled by factor F2 (Pb, Sb, Cu, Zn, Co) or have
438 small F2 loadings (< 0.5) which are opposite in sign to expectations (Se, Mo). This
439 apparent inconsistency can be explained by the fact that most of these elements are more
440 strongly controlled by other factors, such as depositional temperature (Pb, Sb, Cu, Se,
441 Co) and zone refining processes (Zn, Co; see below). Therefore, the influence of r/w ratio
442 on these elements may not be apparent in factor F2. As for Mo and Se, their model
443 concentrations at high r/w ratios (Fig. 5) are probably overestimated, because the model
444 does not allow for their incorporation in alteration silicates and sulfides, which may
445 contain significant traces of these elements (Wedepohl, 1969). Expecting an enrichment
446 in these elements at high r/w ratios is therefore unwarranted. Our thermodynamic models
447 do not consider possible kinetic effects, which may strongly influence fluid chemistry in
448 ultramafic-hosted systems at high temperature (Allen and Seyfried, 2003). However, they

449 suggest a possible mechanism for (Au, Ag)–Ni decoupling, which may be effective at
450 least under near-equilibrium conditions in both mafic and ultramafic substrates.

451 It is noteworthy that in both basalt–seawater and peridotite–seawater systems, fO_2
452 is predicted to decrease at high r/w ratios as a consequence of alteration of ferrous Fe-
453 bearing silicates (Fig. 5). Thus, the association between high dissolved H_2, negative F2
454 loading and high Au grade in many hydrothermal sites on slow-spreading ridges (Fig. 4A
455 and 6) may at least in part be a consequence of reactions between seawater and substrate
456 rocks at relatively high r/w ratios rather than of reactions of seawater with specific
457 lithologies. The dispersion of F2 values for both slow- and intermediate/fast-spreading
458 ridges (Fig. 4A) reveals intra-ridge or even within-site geochemical variations, which can
459 be ascribed to minor changes in space and time of hydrothermal circuits and r/w ratios. A
460 similar interpretation was proposed by Bach and Humphris (1999) to explain variations in
461 Sr and O isotope compositions of seafloor hydrothermal fluids.

462 Based on the results of thermodynamic modeling at 400 °C, the r/w ratios that
463 would be the most significant in determining the observed compositional variability
464 range from ~0.002 to 1, i.e., from log(r/w) –2.7 to log(r/w) 0 (Fig. 5). Within this range, a
465 steady increase of dissolved Au and Ag is accompanied by constant or even decreasing
466 Ni concentrations due to its incorporation into secondary silicates and sulfides. This
467 range is compatible with the r/w ratios <1 to << 1 estimated for seafloor hydrothermal
468 systems from experiments on hydrothermal alteration of seafloor rocks (Seyfried et al.,
469 1988). Note that our r/w ratios refer to conditions in the reaction zone and thus are not
470 directly comparable with the 'integrated' ratios calculated from geochemical data on vent

fluids (B and Sr isotopes, Li/Cl ratios) and from geophysical data, which suggest a typical range of ~0.3–2 (Mottl, 2003; Seyfried and Shanks, 2004; Barker et al., 2010).

4.3 The effect of zone refining

Factor F3 explains 9% of the variability and discriminates Zn-rich, Co-Mo-poor assemblages from those that are poor in Zn but relatively enriched in Co and Mo (Fig. 3 and 4B). We interpret this anti-correlation to be related to zone refining processes. During zone refining, mixing of hydrothermal fluid with seawater within the sulfide mound leads to dissolution of earlier Zn-sulfides and precipitation of pyrite, anhydrite and chalcopyrite, producing moderate temperature fluids enriched in Zn (and Au, Ag, Sb, Pb, and Cd). These fluids may vent from white smokers, in which abundant sphalerite is re-precipitated (Edmond et al., 1995; Tivey et al., 1995; Hannington, 2014). Consistently, samples of white smoker chimneys from TAG show high F3 scores (Fig. S2). Cobalt and, especially, Mo are mainly stored in Fe sulfides, and pyrite in particular (up to several thousand or several hundred ppm, respectively; Maslennikov et al., 2009; Keith et al., 2016). Chalcopyrite can also host significant Co (up to several thousand ppm; Maslennikov et al., 2017). Therefore, Co and Mo are likely to remain relatively immobile during zone refining and, consistently, they show negative F3 scores. On the contrary, Ag and Sb, which have small positive loadings in F3, can have high concentrations in sphalerite (hundreds or tens of ppm respectively; Wang et al., 2018) and may be significantly remobilized and, eventually, re-concentrated in newly formed sphalerite near the mound surface. In fact, sphalerite from TAG white smokers have high concentrations of both Ag and Sb (up to >1000 ppm and several hundred ppm,

493 respectively; Tivey et al., 1995). Thus, F3 is likely to represent the effect of metal
494 remobilization on the geochemistry of the hydrothermal fluid.

495 The relatively Zn-rich compositions of some samples from the Main Field on the
496 Juan de Fuca Ridge, which fall in the upper left quadrant in Fig. 4B at high F1 and F3
497 loadings, may have a different origin. They have been ascribed to precipitation from
498 relatively high-temperature but (Cu, Co)-depleted fluids, characterized by a pH higher
499 than typical black smokers due to anomalously high concentrations of ammonia, possibly
500 reflecting hidden organic-rich sedimentary rocks at depth (Tivey et al., 1999). These
501 fluids precipitate Cu-Fe sulfides and then abundant Zn sulfides on conductive cooling
502 within diffusely venting structures. This particular scenario may have produced
503 geochemical associations in the final SMS deposit that are partly similar to those
504 determined by zone refining at other sites.

505 4.4 The role of phase separation, magmatic input and substrate composition

506 The results of our statistical analysis can be explained by factors such as
507 temperature of deposition, ridge spreading rate and varying r/w ratios in the reaction
508 zone, and metal remobilization. If our interpretation is correct, then processes such as
509 phase separation and the input of magmatic fluids, which have sometimes been invoked
510 to explain the compositions of seafloor vent fluids and hydrothermal precipitates
511 (Douville et al., 2002; Melekestseva et al., 2014, 2017; Tivey, 2007), do not play a major

role in determining the overall geochemical variability of SMS on mid-ocean ridges. However, this does not mean that these processes do not occur.

Phase separation is believed to be commonplace in seafloor hydrothermal systems (Coumou et al., 2009). On mid-ocean ridges, it may give rise to vent fluids with different chlorinities and absolute metal contents (Charlou et al., 2002; Hannington et al., 2005; Fouquet et al., 2010; Seyfried et al., 2011). However, experimental studies show that element fractionation due to phase separation strongly depends on sulfur and chloride concentrations (Nagaseki and Hayashi, 2008; Pokrovski et al., 2005, 2008) and will be predictably small at the concentrations typical of seafloor vent fluids (H_2S: 0.5–13 mM, Cl^-: 420–950 mM; Fouquet et al., 2010; Kawasumi and Chiba, 2017). Thus, although in seafloor hydrothermal systems phase separation may certainly influence the absolute concentrations of metals in the fluids, their fractionation between vapor and liquid phases may not be such as to determine significant changes in the final metal-to-metal ratios, which mainly remain controlled by other higher-order factors.

A magmatic fluid input has been specifically invoked to explain the unusual characteristics of some SMS deposits at mid-ocean ridges, such as an anomalous abundance of barite or of silica and Au–Ag (Melekestseva et al., 2014, 2017). Our results are not inconsistent with this explanation. First, barite-rich samples were intentionally discarded in the present work. Second, our statistical analysis is sensitive to overall

statistical trends, but does not discriminate outliers. Therefore, contributions from magmatic fluids that were significant only on a local scale could not be resolved.

One of the most intriguing and unexpected results of this work is that the composition of the substrate does not emerge as a primary factor in determining metal associations in SMS at mid-ocean ridges. We do not deny a possible role of the substrate in producing specific compositional features, but we suggest that, at a global scale, other factors may explain a large proportion of the observed geochemical variability. The fact that ultramafic substrates are restricted to (ultra)slow-spreading ridges may have obscured the role of spreading rate and r/w ratios in many previous evaluations. This may have led to potentially circular arguments, in which the occurrence of particular geochemical features, believed to be ultramafic- (or mafic-) related, in a mafic- (or ultramafic-) hosted deposit were ascribed to the involvement of concealed ultramafic (or mafic) rocks at depth (Marques et al., 2006; Wang et al., 2014; Webber et al., 2015). Some of these features might actually be more strongly related to the r/w ratios and, hence, to the ridge spreading rate.

For instance, it has been argued that the Co/Ni ratio of SMS can be used to discriminate between mafic-dominated and ultramafic-dominated hydrothermal systems (Marques et al., 2006; Zaccarini and Garuti, 2008; Melekestseva et al., 2013). This hypothesis is consistent with the fact that the Co/Ni ratio is significantly higher in MORBs than in ultramafic rocks (0.35 vs. 0.05, calculated from data compiled in Fouquet et al., 2010). Figure 7 shows the relationships between Ni and Co in mafic- and ultramafic-hosted SMS deposits from slow- and intermediate/fast-spreading ridges. The various groups overlap significantly. Thus, although the nature of the substrate (mafic on

554 intermediate/fast-spreading ridges and mafic and ultramafic on slow-spreading ridges) is
555 likely to exert some control on the distribution of Ni and Co in SMS deposits, the Co/Ni
556 ratio overall appears to have little discriminatory power. This suggests that other factors,
557 namely, depositional temperature, r/w ratios in the reaction zone, and zone refining,
558 which may influence to various extent the concentrations of Co and Ni (i.e., F1, F2 and
559 F3 in Fig. 4), may mask the effects of substrate composition when explored through a
560 simple bivariate plot. However, the Co/Ni ratio may be more sensitive in the case of
561 subseafloor stockwork and replacive mineralization, where the local contribution of Ni
562 from ultramafic host-rocks may be significant (cf. Marques et al., 2007). This type of
563 mineralization is not the focus of this work and was in fact excluded from our analysis.

564 Selenium has also been suggested as a potential ultramafic marker based on its
565 higher average content in ultramafic-hosted SMS (Melekestseva et al., 2017), but the
566 ranges of Se concentrations are similar for the mafic- and the ultramafic-hosted deposits
567 (Fuchs et al., 2019). Based on our statistical analysis, Se is strongly related to factor F1,
568 i.e., to the temperature of deposition (Fig. 4). Similar to what suggested by Fouquet et al.
569 (2010) for Cu, the higher average content of Se in sampled ultramafic-hosted SMS may
570 reflect the more diffuse high-temperature discharge and, thus, the widespread enrichment
571 in high-temperature elements at the surface of these deposits.

572 Other features that seem to be typical of ultramafic-hosted SMS cannot be easily
573 explained by factors F1, F2 and F3 and, therefore, have good potential as ultramafic
574 markers. For instance, the median Au/Ag ratio in ultramafic-hosted SMS is five times
575 higher than that in mafic-hosted SMS [$(Au/Ag)_{ultramafic} = 0.072$; $(Au/Ag)_{mafic} = 0.015$], in
576 analogy with Au/Ag in ultramafic rocks vs. MORBs [$(Au/Ag)_{ultramafics} \sim 0.20$;

577 $(Au/Ag)_{MORB}$ ~ 0.020; Anderson, 1989]. The higher Au/Ag in ultramafic-hosted SMS
578 may also reflect the lower pH of fluids produced during peridotite alteration (Fig. 5; see
579 also Allen and Seyfried, 2003), which enhances Ag solubility in the cooling fluid (Fuchs
580 et al., 2019). Another potential marker is Sn, which is systematically enriched in
581 ultramafic-hosted SMS (Fouquet et al., 2010; Evrard et al., 2015; Melekestseva et al.,
582 2017). Because of the scarcity of data for Sn, this element could not be included in our
583 statistical analysis and its significance remains uncertain.

584 Another possibility that would be worth considering is that the fluids that formed
585 *all* SMS deposits on (ultra)slow-spreading ridges interacted with both mafic and
586 ultramafic rocks at depth. This scenario would explain the geochemical similarity
587 between several mafic-hosted and ultramafic-hosted SMS deposits. However, the relative
588 importance of ultramafic rocks vs. r/w ratios in determining the observed geochemical
589 associations would remain difficult to resolve, as these factors are likely to be highly
590 correlated with each other and with the ridge spreading rate.

591 **5 Conclusions**

592 The geochemical associations observed in SMS deposits on mid-ocean ridges can be
593 explained by a combination of the following independent factors, given in order of importance:
594 (1) temperature of deposition, (2) ridge spreading rate and (3) zone refining. The first and the
595 third factors are mostly related to processes that operate near the seafloor, such as conductive
596 cooling and/or mixing with seawater and metal remobilization, and determine the relative
597 proportions of the main minerals and, thus, of Cu and Zn (Co, Se, Sb, Pb). Thus, they are mostly
598 controlled by final depositional conditions and evolution of mound and vent structures rather

than by the original geochemistry of the hydrothermal fluid. The ridge spreading rate directly influences the structure of the oceanic lithosphere, which in turn exerts a major control on the length and depth of the hydrothermal circuit and on the r/w ratios in the reaction zone, and thus on the behavior of precious metals and Ni (Mo, Se). Despite the obvious role played by substrate rocks in releasing elements to hydrothermal fluids, their nature (specifically mafic vs. ultramafic) does not clearly emerge as a statistically significant independent factor. Therefore, using simple parameters such as metal grades or bivariate metal ratios to discriminate between mafic and ultramafic hydrothermal systems may lead to erroneous evaluations. In any case, the relative importance of highly correlated factors such as r/w and ultramafic/mafic volume ratios in the reaction zone may be difficult to resolve using simple compositional data. The composition of the substrate, however, may become relevant in subseafloor mineralization, where sulfides precipitate by reaction of ascending hydrothermal fluids with substrate host-rocks. On a global scale, widely recognized processes such as phase separation and magmatic fluid input do not appear to play a major role in determining the overall geochemical diversity of SMS deposits on mid-ocean ridges. These processes may nevertheless have a significant influence on a small time-space scale, and may rather be reflected by peculiar mineral assemblages (e.g., barite-rich or silica and Au-rich), which are only found at specific sites.

Acknowledgments

This work is part of L.T.'s post-doctoral project at the Università di Padova. G.A.T. and I.Yu.M acknowledge financial support by the South Urals Federal Research Center, Urals Branch of Russian Academy of Sciences, Institute of Mineralogy (grant number AAAA-A-19-119061790049-3). The authors are grateful to the crew of *R/V Professor Logatchev* (Polar Marine Geosurvey Expedition, Lomonosov-St. Petersburg) for sampling the Irinovskoe, Krasnov

622 and Peterburgskoe SMS fields. We are grateful to T. Monecke and two anonymous reviewers for
623 their careful reading and constructive comments, which helped us to improve the manuscript.

624 **References**

625 Allen, D.E., Seyfried, Jr., W.E, 2003. Compositional controls on vent fluids from ultramafic-
626 hosted hydrothermal systems at mid-ocean ridges: An experimental study at 400°C, 500
627 bars. Geochim. Cosmochim. Acta 67, 1531–1542.

628 Alt, J.C., Honnorez, J., Laverne, C., Emmermann, R., 1986. Hydrothermal alteration of a 1 km
629 section through the upper oceanic crust, Deep Sea Drilling Project hole 504B:
630 Mineralogy, chemistry, and evolution of seawater-basalt interactions. J. Geophys. Res.
631 91, 10309–10335.

632 Ames, D.E., Franklin, J.M., Hannington, M.D., 1993. Mineralogy and geochemistry of active
633 and inactive chimneys and massive sulfide, Middle Valley, northern Juan de Fuca Ridge;
634 an evolving hydrothermal system. Can. Mineral. 31, 997–1024.

635 Anderson, D.L., 1989. Composition of the Earth. Science 243, 367–370.

636 Bach, W., Humphris, S.E., 1999. Relationship between the Sr and O isotope compositions of
637 hydrothermal fluids and the spreading and magma-supply rates at oceanic spreading
638 centers. Geology 27, 1067–1070.

639 Bäcker, H., Lange, J., Marchig, V., 1985. Hydrothermal activity and sulphide formation in axial
640 valleys of the East Pacific Rise crest between 18° S and 22° S. Earth Planet. Sci. Lett. 72,
641 9–22.

642 Barker, A.K., Coogan, L.A., Gillis, K.M., 2010. Insights into the behavior of sulphur in mid-
643 ocean ridge axial hydrothermal systems from the composition of the sheeted dyke
644 complex at Pito Deep. Chem. Geol. 275, 105–115.

645 Barrett, T.J., Jarvis, I., Jarvis, K.E., 1990. Rare earth element geochemistry of massive sulfides-
646 sulfates and gossans on the Southern Explorer Ridge. Geology 18, 583–586.

647 Becker, K.P., 1987. Die massiven sulfiderze des Galapagos Rifts mineralogisch-geochemische
648 untersuchungen. Unpublished M. Sc. Thesis, Institut für Mineralogie und
649 Lagerstättenlehre, RWTH Aachen, Germany, 105 pp.

650 Benninger, L.M., Koski, R.A., 1987. Descriptions and chemical analyses of sulfide samples
651 dredged in 1986 from Escanaba Trough, southern Gorda Ridge (No. 87-375-B). US
652 Geological Survey.

653 Bischoff, J.L., Rosenbauer, R.J., Aruscavage, P.J., Baedecker, P.A., Crock, J.G., 1983. Sea-floor
654 massive sulfide deposits from 21° N East Pacific Rise, Juan de Fuca Ridge, and
655 Galapagos Rift; bulk chemical composition and economic implications. Econ. Geol. 78,
656 1711–1720.

657 Bougault, H., Charlou, J.L., Fouquet, Y., Needham, H. ., Vaslet, N., Appriou, P., Jean Baptiste,
658 P., Rona, P.A., Dmitriev, L., Silantiev, S., 1993. Fast and slow spreading ridges: structure
659 and hydrothermal activity, ultramafic topographic highs, and CH_4 output. J. Geophys.
660 Res. Solid Earth 98, 9643–9651.

661 Campbell, A. C., Palmer, M. R., Klinkhammer, G.P., Bowers, T. S., Edmond, J. M., Lawrence, J.
662 R., Casey, J. F., Thompson, G., Humphris, S., Rona, P., & Karson, J. A., (1988).
663 Chemistry of hot springs on the Mid-Atlantic Ridge. Nature, 335, 514–519.

664 Charlou, J.L., Donval, J.P., Jean-Baptiste, P., Dapoigny, A., Rona, P.A., 1996. Gases and helium
665 isotopes in high temperature solutions samples before and after ODP Leg 158 drilling at
666 TAG hydrothermal field (26°N,MAR). Geophys. Res. Lett. 23, 3491–3494.

667 Charlou, J.L., Donval, J.P., Fouquet, Y., Jean-Baptiste, P., Holm, N., 2002. Geochemistry of
668 high H_2 and CH_4 vent fluids issuing from ultramafic rocks at the Rainbow hydrothermal
669 field (36 14′ N, MAR). Chem. Geol. 191, 345–359.

670 Chudnenko K.V., 2010. Thermodynamic modeling in geochemistry: theory, algorithms,
671 software, and applications. Geo, Novosibirsk, 287 pp. [in Russian]

672 Cook, N.J., Ciobanu, C.L., Pring, A., Skinner, W., Shimizu, M., Danyushevsky, L., Saini-
673 Eidukat, B., Melcher, F., 2009. Trace and minor elements in sphalerite: a LA-IC-MS
674 study. Geochim. Cosmochim. Acta 73, 4761–4791.

675 Coumou, D., Driesner, T., Heinrich, C.A., 2008. The structure and dynamics of mid-ocean ridge
676 hydrothermal systems. Science 321, 1825–1828.

677 Coumou, D., Driesner, T., Weis, P., Heinrich, C.A., 2009. Phase separation, brine formation, and
678 salinity variation at Black Smoker hydrothermal systems. J. Geophys. Res. Solid Earth
679 114, B03212.

680 da Cruz, M.I.F.S., 2015. Mineralogy and geochemistry of contrasting hydrothermal systems on
681 the Arctic Mid Ocean Ridge (AMOR): the Jan Mayen and Loki's Castle vent fields. PhD
682 thesis, Universidade de Lisboa, Portugal, 257 pp.

683 Douville, E., Charlou, J.-L., Oelkers, E.H., Bienvenu, P., Colon, C.F.J., Donval, J.P., Fouquet,
684 Y., Prieur, D., Appriou, P., 2002. The Rainbow vent fluid (36◦14′N, MAR): the influence

685 of ultramafic rocks and phase separation on trace metal content in Mid-Atlantic Ridge
686 hydrothermal fluids. Chem. Geol. 184, 37–48.

687 Edmond, J.M.A., Campbell, C., Palmer, M.R., German, C.R., Klinkhammer, G.P., Edmonds,
688 H.N., Elderfield, H., Thompson, G., Rona, P., 1995. Time series studies of vent fluids
689 from the TAG and MARK sites (1986, 1990) Mid-Atlantic Ridge and a mechanism for
690 Cu/Zn zonation in massive sulphide orebodies. In: Parson, L.M., Walker, C.L., Dixon,
691 D.R. (Eds.), Hydrothermal Vents and Processes. Geol. Soc. Lond., Spec. Publ. 87, 77–86.

692 Embley, R.W., Jonasson, I.R., Perfit, M.R., Franklin, J.M., Tivey, M.A., Malahoff, A., Smith,
693 M.F., Francis, T.J.G., 1988. Submersible investigation of an extinct hydrothermal system
694 on the Galapagos Ridge; sulfide mounds, stockwork zone, and differentiated lavas. Can.
695 Mineral.. 26, 517–539.

696 Evrard, C., Fouquet, Y., Moelo, Y., Rinnert, E., Etoubleau, J., Langlade, J.A., 2015. Tin
697 concentration in hydrothermal sulfides related to ultramafic rocks along the Mid-Atlantic
698 Ridge: a mineralogical study. Eur. J. Mineral. 27, 627–638.

699 Filzmoser, P., Hron, K., 2011. Robust statistical analysis. In: Pawlowsky-Glahn, V., Buccianti,
700 A. (Eds.), Compositional data analysis. Theory and applications. John Wiley & Sons,
701 Chichester (UK), pp. 59–72.

702 Filzmoser, P., Hron, K., Reimann, C., Garrett, R., 2009a. Robust factor analysis for
703 compositional data. Computers & Geosciences 35, 1854–1861.

704 Filzmoser, P., Hron., K, Reimann, C., 2009b. Principal component analysis for compositional
705 data with outliers. Environmetrics 20, 621–632.

706 Fouquet, Y., Auclair, G., Cambon, P., Etoubleau, J., 1988. Geological setting and mineralogical
707 and geochemical investigations on sulfide deposits near 13° N on the East Pacific Rise.
708 Marine Geol. 84, 145–178.

709 Fouquet, Y., Cambon, P., Etoubleau, J., Charlou, J.L., Ondréas, H., Barriga, F.J., Cherkashov,
710 G., Semkova, T., Poroshina, I., Bohn, M., Donval, J.P., Henry, K., Murphy, P., Rouxel,
711 O., 2010. Geodiversity of hydrothermal processes along the Mid-Atlantic Ridge and
712 ultramafic-hosted mineralization: a new type of oceanic Cu-Zn-Co-Au volcanogenic
713 massive sulfide deposit. In: Rona, P.A., Devey, C.W., Dyment, J., Murton, B.J. (Eds.),
714 Diversity of Hydrothermal Systems on Slow Spreading Ocean Ridges. Geophysical
715 Monograph, 188. American Geophysical Union, Washington DC, pp. 321–367.

716 Francheteau, J., Needham, H.D., Choukroune, P., Juteau, T., Séguret, M., Ballard, R.D., Fox,
717 P.J., Normark, W., Carranza, A., Cordoba, D., Guerrero, J., Rangin, C., Bougault, H.,
718 Cambon P., Hekinian, R., 1979. Massive deep sea sulphide ore deposit discovered on the
719 East Pacific Rise. Nature 277, 523–528.

720 Fuchs, S., Hannington, M.D., Petersen, S., 2019. Divining gold in seafloor polymetallic massive
721 sulfide systems. Mineral. Deposita 54, 789–820.

722 Gallant, R.M., Von Damm, K.L., 2006. Geochemical controls on hydrothermal fluids from the
723 Kairei and Edmond Vent Fields, 23°–25°S, Central Indian Ridge. Geochem. Geophys.
724 Geosystems 7, Q06018.

725 German, C.R., Petersen, S., Hannington, M.D., 2016. Hydrothermal exploration of mid-ocean
726 ridges: where might the largest sulfide deposits be forming? Chem. Geol. 420, 114–126.

727 Grant, H.L., Hannington, M.D., Petersen, S., Frische, M., Fuchs, S.H., 2018. Constraints on the
728 behavior of trace elements in the actively-forming TAG deposit, Mid-Atlantic Ridge,
729 based on LA-ICP-MS analyses of pyrite. Chem. Geol. 498, 45–71.
730 Halbach, P., Auzende, J.M., Tuerkay, M., Allspach, A., Becker, K. et al., 1996. The Indian
731 Ocean, future area for drilling activities. Poster-Eurocolloquium-ODP Meeting, pp. 47–
732 48.
733 Halbach, P., Blum, N., Münch, U., Plüger, W., Garbe-Schönberg, D., Zimmer, M., 1998.
734 Formation and decay of a modern massive sulfide deposit in the Indian Ocean. Mineral.
735 Deposita 33, 302–309.
736 Hannington, M.D., 1989. The geochemistry of gold in modern seafloor hydrothermal systems
737 and implication for gold mineralization in ancient volcanogenic massive sulfides.
738 Unpublished PhD thesis, University of Toronto, Canada, 544 pp.
739 Hannington, M.D., 2014. Volcanogenic massive sulfide deposits. In: Scott, S.D. (Ed.), Treatise
740 on geochemistry, Vol. 13: geochemistry of mineral deposits. Elsevier, Amsterdam, 2nd
741 ed., pp. 463–488.
742 Hannington, M., Herzig, P., Scott, S., Thompson, G., Rona, P., 1991a. Comparative mineralogy
743 and geochemistry of gold-bearing sulfide deposits on the mid-ocean ridges. Marine Geol.
744 101, 217–248.
745 Hannington, M.D., Herzig, P.M., Scott, S.D., 1991b. Auriferous hydrothermal precipitates on the
746 modern seafloor. In: Foster, R. P. (Ed.), Gold Metallogeny and Exploration. Blackie and
747 Son, Glasgow, pp. 249−282.

748 Hannington, M.D., Tivey, M.K., Larocque, A.C., Petersen, S., Rona, P., 1995. The occurrence of
749 gold in sulfide deposits of the TAG Hydrothermal Field, Mid-Atlantic Ridge. Can.
750 Mineral.. 33, 1285–1310.

751 Hannington, M.D., Petersen, S., Herzig, P.M., Jonasson, I.R., 2004. A global database of
752 seafloor hydrothermal systems, including a digital database of geochemical analyses of
753 seafloor polymetallic sulfides. Geological Survey of Canada, Open File 4598, 1 CD-
754 ROM.

755 Hannington, M.D., de Ronde, C.E.J., Petersen, S., 2005. Sea-floor tectonics and submarine
756 hydrothermal systems. Econ. Geol. 100th Anniversary Volume, pp. 111–141.

757 Hannington, M.D., Jamieson, J., Monecke, T., Petersen, S., Beaulieu, S., 2011. The abundance of
758 seafloor massive sulfide deposits. Geology 39, 1155–1158.

759 Holwell, D.A., Adeyemi, Z., Ward, L.A., Smith, D.J., Graham, S.D., McDonald, I., Smith, J.W.,
760 2017. Low temperature alteration of magmatic Ni-Cu-PGE sulfides as a source for
761 hydrothermal Ni and PGE ores: A quantitative approach using automated mineralogy.
762 Ore Geol. Rev. 91, 718–740.

763 Huston, D.L., Sie, S.H., Suter, G.F., Cooke, D.R., Both, R.A., 1995. Trace elements in sulfide
764 minerals from eastern Australian volcanic-hosted massive sulfide deposits: Part I. Proton
765 microprobe analyses of pyrite, chalcopyrite, and sphalerite, and Part II. Selenium levels
766 in pyrite: comparison with $\delta^{34}S$ values and implications for the source of sulfur in
767 volcanogenic hydrothermal systems. Econ. Geol. 90, 1167–1196.

768 Janecky, D.R., Seyfried Jr., W.E., 1984. Formation of massive sulfide deposits on oceanic ridge
769 crests: Incremental reaction models for mixing between hydrothermal solutions and
770 seawater. Geochim. Cosmochim. Acta 48, 2723–2738.

771 Janecky, D.R., Seyfried Jr., W.E., 1986. Hydrothermal serpentinization of peridotite within the
772 oceanic crust: Experimental investigations of mineralogy and major element chemistry.
773 Geochim. Cosmochim. Acta 50, 1357–1378.

774 Jean-Baptiste, P., Charlou, J.L., Stievenard, M., Donval, J.P., Bougault, H., Mevel, C., 1991.
775 Helium and methane measurements in hydrothermal fluids from the Mid-Atlantic Ridge:
776 the Snake Pit site at 23° N. Earth Planet. Sci. Lett. 106, 17-28.

777 Karpov, I.K., Chudnenko, K.V., Kulik, D.A., 1997. Modeling chemical mass transfer in
778 geochemical processes: Thermodynamic relations, conditions of equilibrium, and
779 numerical algorithms. Am. J. Sci. 297, 767–806.

780 Kawasumi, S., Chiba, H., 2017. Redox state of seafloor hydrothermal fluids and its effect on
781 sulfide mineralization. Chem. Geol. 451, 25–37.

782 Keith, M., Häckel, F., Haase, K.M., Schwarz-Schampera, U., Klemd, R., 2016. Trace element
783 systematics of pyrite from submarine hydrothermal vents. Ore Geol. Rev. 72, 728–745.

784 Klein, F., Bach, W., 2009. Fe–Ni–Co–O–S phase relations in peridotite–seawater interactions. J.
785 Petrol. 50, 37-59.

786 Klein, F., Bach, W., McCollom, T.M., 2013. Compositional controls on hydrogen generation
787 during serpentinization of ultramafic rocks. Lithos 178, 55-69.

788 Knight, R.D., Roberts, S., Webber, A.P., 2018. The influence of spreading rate, basement
789 composition, fluid chemistry and chimney morphology on the formation of gold-rich
790 SMS deposits at slow and ultraslow mid-ocean ridges. Mineral. Deposita 53, 143–152.

791 Koski, R.A., Shanks, W.C., Bohrson, W.A., Oscarson, R.L., 1988. The composition of massive
792 sulfide deposits from the sediment-covered floor of Escanaba Trough, Gorda Ridge;
793 implications for depositional processes. Can. Mineral. 26, 655–673.

794 Koski, R.A., Benninger, L.M., Zierenberg, R.A., Jonasson, I.R., 1994. Composition and growth
795 history of hydrothermal deposits in Escanaba Trough, southern Gorda Ridge. In: Morton,
796 J.L., Zierenberg, R.A., Riess, C.A. (Eds.), Geologic, Hydrothermal, and Biologic Studies
797 at Escanaba Trough, Gorda Ridge, Offshore Northern California. U.S. Geological Survey
798 Bulletin 2022, pp. 293–324.

799 Krasnov, S.G., Poroshina, I.M., Cherkashev, G.A., 1995. Geological setting of high-temperature
800 hydrothermal activity and massive sulphide formation on fast- and slow-spreading ridges.
801 In: Parson, L.M., Walker, C.L., Dixon, D.R. (Eds.), Hydrothermal Vents and Processes.
802 Geol. Soc. Lond., Spec. Publ. 87, 17–23.

803 Kumagai, H., Nakamura, K., Toki, T., Morishita, T., Okino, K., Ishibashi, J.I., Tsunogai, U.,
804 Kawagucci, S., Gamo, T., Shibuya, T., Sawaguchi, T., Neo, N., Joshima, M., Sato, T.,
805 Takai, K., 2008. Geological background of the Kairei and Edmond hydrothermal fields
806 along the Central Indian Ridge: implications of their vent fluids' distinct chemistry.
807 Geofluids 8, 239–251.

808 Lehnert, K., Su Y., Langmuir, C., Sarbas, B., Nohl, U., 2000. A global geochemical database
809 structure for rocks. Geochem. Geophys. Geosystems 1, 1–14.

Liu, W., Migdisov, A., Williams-Jones, A., 2012. The stability of aqueous nickel (II) chloride complexes in hydrothermal solutions: Results of UV–Visible spectroscopic experiments. Geochim. Cosmochim. Acta 94, 276–290.

Lowell, R., 2010. Hydrothermal circulation at slow spreading ridges: analysis of heat sources and heat transfer processes. In: Rona, P.A., Devey, C.W., Dyment, J., Murton, B.J. (Eds.), Diversity of Hydrothermal Systems on Slow Spreading Ocean Ridges. Geophysical Monograph, 188. American Geophysical Union, Washington DC, pp. 11–26.

Lowell, R.P., Rona, P.A., Von Herzen, R.P., 1995. Seafloor hydrothermal systems. J. Geophys. Res. Solid Earth 100, 327–352.

MacLeod, C.J., Searle, R.C., Murton, B.J., Casey, J.F., Mallows, C., Unsworth, S.C., Achenbach, K.L., Harris, M., 2009. Life cycle of oceanic core complexes. Earth Planet. Sci. Lett. 287, 333–344.

Marchig, V., Blum, N., Roonwal, G., 1997. Massive sulfide chimneys from the east pacific rise at 7 24's and 16 43's. Marine Georesources & Geotechnology 15, 49–66.

Marques, A.F.A., Barriga, F.J.A.S., Chavagnac, V., Fouquet, Y., 2006. Mineralogy, geochemistry, and Nd isotope composition of the Rainbow hydrothermal field, Mid-Atlantic Ridge. Mineral. Deposita 41, 52–67.

Marques, A.F.A., Barriga, F.J.A.S, Scott, S.D., 2007. Sulfide mineralization in an ultramafic-rock hosted seafloor hydrothermal system: From serpentinization to the formation of Cu–Zn–(Co)-rich massive sulfides. Marine Geol. 245, 20–39.

831 Martín-Fernández, J.A., Barceló-Vidal, C., Pawlowsky-Glahn, V., 2003. Dealing with zeros and
832 missing values in compositional data sets using nonparametric imputation. Math. Geol.
833 35, 253–278.

834 Maslennikov, V.V., Maslennikova, S.P., Large, R.R., Danyushevsky, L., 2009. Study of trace
835 element zonation in vent chimneys from the Silurian Yaman-Kasy volcanic-hosted
836 massive sulfide deposit (Southern Urals, Russia) using laser ablation-inductively coupled
837 plasma mass spectrometry (LA-ICPMS). Econ. Geol. 104, 111–141.

838 Maslennikov, V.V., Maslennikova, S.P., Large, R.R., Danyushevsky, L.V., Herrington, R.J.,
839 Ayupova, N.R., Zaykov, V.V., Lein, A.Yu., Tseluyko, A.S., Melekestseva, I.Yu.,
840 Tessalina, S.G., 2017. Chimneys in Paleozoic massive sulfide mounds of the Urals VMS
841 deposits: Mineral and trace element comparison with modern black, grey, white and clear
842 smokers. Ore Geol. Rev. 85, 64–106.

843 McCollom, T.M., Shock, E.L., 1998. Fluid-rock interactions in the lower oceanic crust:
844 Thermodynamic models of hydrothermal alteration. J. Geophys. Res. Solid Earth
845 103(B1), 547–575.

846 McDermott, J.M., Sylva, S.P., Ono, S., German, C.R., Seewald, J.S., 2018. Geochemistry of
847 fluids from Earth's deepest ridge-crest hot-springs: Piccard hydrothermal field, Mid-
848 Cayman Rise, Geochim. Cosmochim. Acta 228, 95–118.

849 Melekestseva, I.Yu., Zaykov, V.V., Nimis, P., Tret'yakov, G.A., Tesalina, S.G., 2013. Cu-(Ni-
850 Co-Au)–bearing massive sulfide deposits associated with mafic-ultramafic rocks of the
851 Main Urals fault, South Urals: Geological structures, ore textural and mineralogical
852 features, comparison with modern analogs. Ore Geol. Rev. 52, 18–36.

853 Melekestseva, I.Yu., Tret'yakov, G.A., Nimis, P., Yuminov, A.M., Maslennikov, V.V.,
854 Maslennikova, S.P., Kotlyarov, V.A., Beltenev, V.E., Danyushevsky, L.V., Large, R.,
855 2014. Barite-rich massive sulfides from the Semenov-1 hydrothermal field (Mid-Atlantic
856 Ridge, 13°30.87'N): Evidence for phase separation and magmatic input. Marine Geol.
857 349, 37–54.

858 Melekestseva, I.Yu., Maslennikov, V.V., Tret'yakov, G.A., Nimis, P., Beltenev, V.E.,
859 Rozhdestvenskaya, I.I., Maslennikova, S.P., Belogub, E.V., Danyushevsky, L., Large, R.,
860 Yuminov, A.M., Sadykov, S.A., 2017. Gold-and Silver-Rich Massive Sulfides from the
861 Semenov-2 Hydrothermal Field, 13° 31.13'N, Mid-Atlantic Ridge: A Case of Magmatic
862 Contribution? Econ. Geol. 112, 741–773.

863 Moss, R., Scott, S.D., 1996. Silver in sulfide chimneys and mounds from 13° N and 21° N, East
864 Pacific Rise. Can. Mineral. 34, 697–716.

865 Mottl, M.J., 2003. Partitioning of energy and mass fluxes between mid-ocean ridges axes and
866 flanks at high and low temperature. In: Halbach, P.E., Tunnicliffe, V., Hein, J.R. (Eds.),
867 Energy and Mass Transfer in Marine Hydrothermal Systems. Dahlem University Press,
868 Berlin, pp. 271–286.

869 Murphy, P.J., Meyer, G., 1998. A gold-copper association in ultramafic-hosted hydrothermal
870 sulfides from the Mid-Atlantic Ridge. Econ. Geol. 93, 1076–1083.

871 Nagaseki, H., Hayashi, K.I., 2008. Experimental study of the behavior of copper and zinc in a
872 boiling hydrothermal system. Geology 36, 27–30.

873 Palandri, J.L., Reed, M.H., 2004. Geochemical models of metasomatism in ultramafic systems:
874 Serpentinization, rodingitization, and sea floor carbonate chimney precipitation.
875 Geochim. Cosmochim. Acta 68, 1115–1133.

876 Palarea-Albaladejo, J., Martín-Fernández, J.A., 2015. zCompositions—R package for
877 multivariate imputation of left-censored data under a compositional approach.
878 Chemometrics and Intelligent Laboratory Systems 143, 85–96.

879 Patten, C.G., Pitcairn, I.K., Teagle, D.A., Harris, M., 2016. Sulphide mineral evolution and metal
880 mobility during alteration of the oceanic crust: Insights from ODP Hole 1256D.
881 Geochim. Cosmochim. Acta 193, 132–159.

882 Pester, N.J., Rough, M., Ding, K., Seyfried, W.E., 2011. A new Fe/Mn geothermometer for
883 hydrothermal systems: implications for high-salinity fluids at 13°N on the East Pacific
884 Rise. Geochim. Cosmochim. Acta 75, 7881–7892.

885 Petersen, S., 2000. The Geochemical and Mineralogical Evolution of the TAG Hydrothermal
886 field, Mid-Atlantic Ridge, 26° N. Unpublished PhD thesis, TU Bergakademie Freiberg,
887 Freiberg, Germany.

888 Petersen, S., Hein, J.R., 2013. The geology of sea-floor massive sulphides. In: Baker, E.,
889 Beaudoin, Y. (Eds.), Deep Sea Minerals: Sea-floor Massive Sulphides, a Physical,
890 Biological, Environmental, and Technical Review. Vol. 1A, Secretariat of the Pacific
891 Community.

892 Pokrovski, G.S., Roux, J., Harrichoury, J.C., 2005. Fluid density control on vapor-liquid
893 partitioning of metals in hydrothermal systems. Geology 33, 657–660.

894 Pokrovski, G.S., Borisova, A.Y., Harrichoury, J.C., 2008. The effect of sulfur on vapor–liquid
895 fractionation of metals in hydrothermal systems. Earth Planet. Sci. Lett. 266, 345–362.
896 Reimann, C., Filzmoser, P., Garrett, R.G., 2002. Factor analysis applied to regional geochemical
897 data: problems and possibilities. Appl. Geochem. 17, 185–206.
898 Reimann, C., Filzmoser, P., Garrett, R.G., Dutter, R., 2008. Statistical Data Analysis Explained:
899 Applied Environmental Statistics with R. John Wiley & Sons, Chichester, UK, 343 pp.
900 Rona, P.A., Bogdanov, Y.A., Gurvich, E.G., Rimski-Korsakov, N.A., Sagalevitch, A.M.,
901 Hannington, M.D., Thompson, G., 1993. Relict hydrothermal zones in the TAG
902 hydrothermal field, Mid-Atlantic Ridge 26° N, 45° W. J. Geophys. Res. Solid Earth 98,
903 9715–9730.
904 Safina, N.P., Melekestseva, I.Yu., Nimis, P., Ankusheva, N.N., Yuminov, A.M., Kotlyarov,
905 V.A., Sadykov, S.A., 2016. Barite from the Saf'yanovka VMS deposit (Central Urals)
906 and Semenov-1 and -3 hydrothermal sulfide fields (Mid-Atlantic Ridge): A comparative
907 analysis of formation conditions. Mineral. Deposita 51, 491–507.
908 Samson, J., 1986. Compilation of information on polymetallic sulfide deposits and occurrences
909 off the west coast of Canada. Canada Oil and Gas Lands Administration, pp. 1–58.
910 Sharp, T.G., Buseck, P.R., 1993. The distribution of Ag and Sb in galena: Inclusions versus solid
911 solution. Am. Mineral. 78, 85–95.
912 Seewald, J.S., Seyfried, Jr., W.E., 1990. The effect of temperature on metal mobility in
913 subseafloor hydrothermal systems: constraints from basalt alteration experiments. Earth
914 Planet. Sci. Lett. 101, 388–403.

915 Seewald, J.S., Cruse, A.M., Saccocia, P.J., 2003. Aqueous volatiles in hydrothermal fluids from
916 the Main Endeavour Field, northern Juan de Fuca Ridge: temporal variability following
917 earthquake activity. Earth Planet. Sci. Lett. 216, 575–590.

918 Seyfried, W., Bischoff, J.L., 1977. Hydrothermal transport of heavy metals by seawater: the role
919 of seawater/basalt ratio. Earth Planet. Sci. Lett. 34, 71–77.

920 Seyfried, Jr., W.E., Bischoff, J.L., 1981. Experimental seawater-basalt interaction at 300° C, 500
921 bars, chemical exchange, secondary mineral formation and implications for the transport
922 of heavy metals. Geochim. Cosmochim. Acta 45, 135–147.

923 Seyfried, Jr., W.E., Dibble Jr., W.E., 1980. Seawater-peridotite interaction at 300 °C and 500
924 bars: implications for the origin of oceanic serpentinites. Geochim. Cosmochim. Acta 44,
925 309–321.

926 Seyfried, W.E., Ding, K., 1995. Phase equilibria in subseafloor hydrothermal systems: A review
927 of the role of redox, temperature, pH and dissolved Cl on the chemistry of hot spring
928 fluids at mid-ocean ridges. In: Humphris, S.E., Zierenberg, R.A., Mullineaux, L.S.,
929 Thomson, R.E. (Eds.), Seafloor Hydrothermal Systems: Physical, Chemical, Biological,
930 and Geological Interactions, AGU Geophysical Monograph, vol. 91, pp. 248–272.

931 Seyfried, Jr., W.E., Janecky, D.R., 1985. Heavy metal and sulfur transport during subcritical and
932 supercritical hydrothermal alteration of basalt: Influence of fluid pressure and basalt
933 composition and crystallinity. Geochim. Cosmochim. Acta 49, 2545–2560.

934 Seyfried, Jr., W.E., Mottl, M.J., 1982. Hydrothermal alteration of basalt by seawater under
935 seawater-dominated conditions. Geochim. Cosmochim. Acta 46, 985–1002.

936 Seyfried, Jr., W.E., Shanks, III, W.C., 2004. Alteration and mass transport in mid-ocean ridge
937 hydrothermal systems: Controls on the chemical and isotopic evolution of high-
938 temperature crustal fluids. In: Davis, E., Elderfield, H. (Eds.), Hydrogeology of the
939 Oceanic Lithosphere. Cambridge University Press, Cambridge, pp. 451–495.

940 Seyfried, W.E., Berndt, M.E., Seewald, J.S., 1988. Hydrothermal alteration processes at mid-
941 ocean ridges; constraints from diabase alteration experiments, hot spring fluids and
942 composition of the oceanic crust. Can. Mineral. 26, 787–804.Seyfried, W.E., Seewald,
943 J.S., Berndt, M.E., Ding, K., Foustoukos, D.I., 2003. Chemistry of hydrothermal vent
944 fluids from the Main Endeavour Field, northern Juan de Fuca Ridge: Geochemical
945 controls in the aftermath of June 1999 seismic events. J. Geophys. Res. Solid Earth 108,
946 2429.

947 Seyfried, W.E., Pester, N.J., Ding, K., Rough, M., 2011. Vent fluid chemistry of the Rainbow
948 hydrothermal system (36 N, MAR): Phase equilibria and in situ pH controls on
949 subseafloor alteration processes. Geochim. Cosmochim. Acta 75, 1574–1593.

950 Sleep, N.H., 1983. Hydrothermal convection at ridge axes. In: Rona, P.A., Boström, K., Laubier,
951 L., Smith, K.L.Jr. (Eds.), Hydrothermal Processes of Seafloor Spreading Centers,
952 Springer-Verlag, New York, pp. 71–82.

953 Steele, J.H., Thorpe, S.A., Turekian, K.K., eds., 2010. Encyclopedia of ocean sciences, second
954 edition: Appendix 3, Estimated mean oceanic concentration of the elements: Amsterdam,
955 Elsevier, pp. 602–603.

956 Templ, M., Hron, K., Filzmoser, P., 2011. robCompositions: an R-package for robust statistical
957 analysis of compositional data. In: Pawlowsky-Glahn, V., Buccianti, A. (Eds.),

958 Compositional Data Analysis. Theory and Applications. John Wiley & Sons, Chichester,
959 UK, pp. 341–355.

960 Tivey, M.K., 1995. The influence of hydrothermal fluid composition and advection rates on
961 black smoker chimney mineralogy: insights from modeling transport and reaction.
962 Geochim. Cosmochim. Acta 59, 1933–1949.

963 Tivey, M.K., 2007. Generation of seafloor hydrothermal vent fluids and associated mineral
964 deposits. Oceanography 20, 50–65.

965 Tivey, M.K., Humphris, S.E., Thompson, G., Hannington, M.D., Rona, P.A., 1995. Deducing
966 patterns of fluid flow and mixing within the TAG active hydrothermal mound using
967 mineralogical and geochemical data. J. Geophys. Res. Solid Earth 100(B7), 12527–
968 12555.

969 Tivey, M.K., Stakes, D.S., Cook, T.L., Hannington, M.D., Petersen, S., 1999. A model for
970 growth of steep-sided vent structures on the Endeavour Segment of the Juan de Fuca
971 Ridge: Results of a petrologic and geochemical study. J. Geophys. Res. Solid Earth 104,
972 22859–22883.

973 Vaughan, D.J., Rosso, K.M., 2006. Chemical bonding in sulfide minerals. In: Vaughan D. J.
974 (Ed.), Sulfide mineralogy and geochemistry, Rev. Mineral. Geochem. 61, 231–264.

975 Wang, Y., Han, X., Petersen, S., Jin, X., Qiu, Z., Zhu, J., 2014. Mineralogy and geochemistry of
976 hydrothermal precipitates from Kairei hydrothermal field, Central Indian Ridge. Marine
977 Geol 354, 69–80.

978 Wang, Y., Han, X., Petersen, S., Frische, M., Qiu, Z., Cai, Y., Zhou, P., 2018. Trace metal
979 distribution in sulfide minerals from ultramafic-hosted hydrothermal systems: examples
980 from the Kairei Vent Field, Central Indian Ridge. Minerals 8, 526.

981 Webber, A.P., Roberts, S., Murton, B.J., Hodgkinson, M.R., 2015. Geology, sulfide
982 geochemistry and supercritical venting at the Beebe Hydrothermal Vent Field, Cayman
983 Trough. Geochem. Geophys. Geosystems 16, 2661–2678.

984 Wedepohl, K.H., 1969. Handbook of geochemistry. Springer-Verlag, Berlin, Vol. II.

985 Wetzel, L.R., Shock, E.L., 2000. Distinguishing ultramafic-from basalt-hosted submarine
986 hydrothermal systems by comparing calculated vent fluid compositions. J. Geophys. Res.
987 Solid Earth 105(B4), 8319–8340.

988 Wilcock, W.S., Delaney, J.R., 1996. Mid-ocean ridge sulfide deposits: Evidence for heat
989 extraction from magma chambers or cracking fronts? Earth Planet. Sci. Lett. 145, 49–64.

990 Wohlgemuth-Ueberwasser, C.C., Viljoen, F., Petersen, S., Vorster, C., 2015. Distribution and
991 solubility limits of trace elements in hydrothermal black smoker sulfides: An in-situ LA-
992 ICP-MS study. Geochim. Cosmochim. Acta 159, 16–41.

993 Wu, Z., Sun, X., Xu, H., Konishi, H., Wang, Y., Wang, C., Dai, Y., Deng, X., Yu, M., 2016.
994 Occurrences and distribution of “invisible” precious metals in sulfide deposits from the
995 Edmond hydrothermal field, Central Indian Ridge. Ore Geol. Rev. 79, 105–132.

996 Zaccarini, F., Garuti, G., 2008. Mineralogy and chemical composition of VMS deposits of
997 northern Apennine ophiolites, Italy: evidence for the influence of country rock type on
998 ore composition. Mineral. Petrol. 94, 61–83.

999 Zierenberg, R.A., Shanks, III, W.C., Bischoff, J.L., 1984. Massive sulfide deposits at 21° N, East
1000 Pacific Rise: Chemical composition, stable isotopes, and phase equilibria. Geol. Soc. Am.
1001 Bull. 95, 922–929.
1002

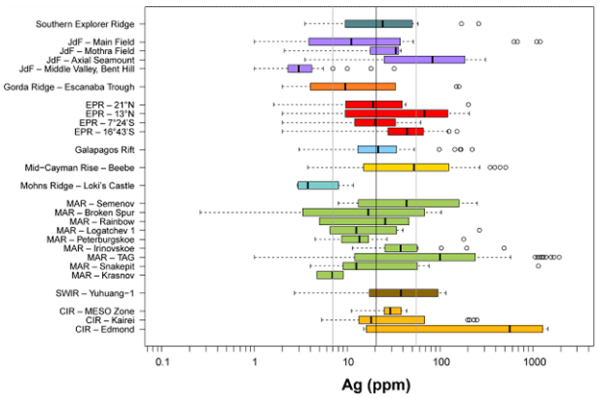
Southern Explorer Ridge
JdF – Main Field
JdF – Mothra Field
JdF – Axial Seamount
JdF – Middle Valley, Bent Hill
Gorda Ridge – Escanaba Trough
EPR – 21°N
EPR – 13°N
EPR – 7°24'S
EPR – 16°43'S
Galapagos Rift
Mid–Cayman Rise – Beebe
Mohns Ridge – Loki's Castle
MAR – Semenov
MAR – Broken Spur
MAR – Rainbow
MAR – Logatchev 1
MAR – Peterburgskoe
MAR – Irinovskoe
MAR – TAG
MAR – Snakepit
MAR – Krasnov
SWIR – Yuhuang–1
CIR – MESO Zone
CIR – Kairei
CIR – Edmond
0.1
1
10
100
1000
Ag (ppm)

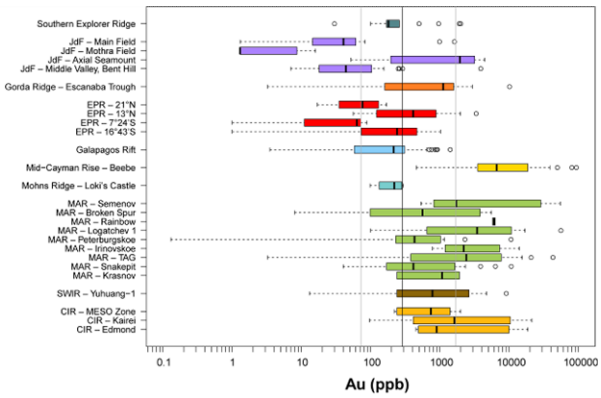
Southern Explorer Ridge
JdF – Main Field
JdF – Mothra Field
JdF – Axial Seamount
JdF – Middle Valley, Bent Hill
Gorda Ridge – Escanaba Trough
EPR – 21°N
EPR – 13°N
EPR – 7°24'S
EPR – 16°43'S
Galapagos Rift
Mid–Cayman Rise – Beebe
Mohns Ridge – Loki's Castle
MAR – Semenov
MAR – Broken Spur
MAR – Rainbow
MAR – Logatchev 1
MAR – Peterburgskoe
MAR – Irinovskoe
MAR – TAG
MAR – Snakepit
MAR – Krasnov
SWIR – Yuhuang–1
CIR – MESO Zone
CIR – Kairei
CIR – Edmond
0.1
1
10
100
1000
10000
100000
Au (ppb)

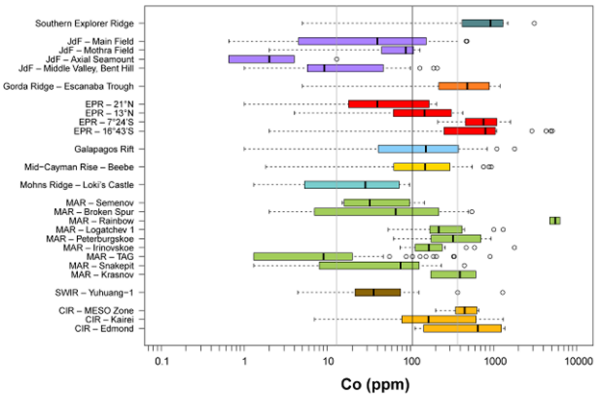
Southern Explorer Ridge
JdF – Main Field
JdF – Mothra Field
JdF – Axial Seamount
JdF – Middle Valley, Bent Hill
Gorda Ridge – Escanaba Trough
EPR – 21°N
EPR – 13°N
EPR – 7°24'S
EPR – 16°43'S
Galapagos Rift
Mid–Cayman Rise – Beebe
Mohns Ridge – Loki's Castle
MAR – Semenov
MAR – Broken Spur
MAR – Rainbow
MAR – Logatchev 1
MAR – Peterburgskoe
MAR – Irinovskoe
MAR – TAG
MAR – Snakepit
MAR – Krasnov
SWIR – Yuhuang–1
CIR – MESO Zone
CIR – Kairei
CIR – Edmond
0.1
1
10
100
1000
10000
Co (ppm)

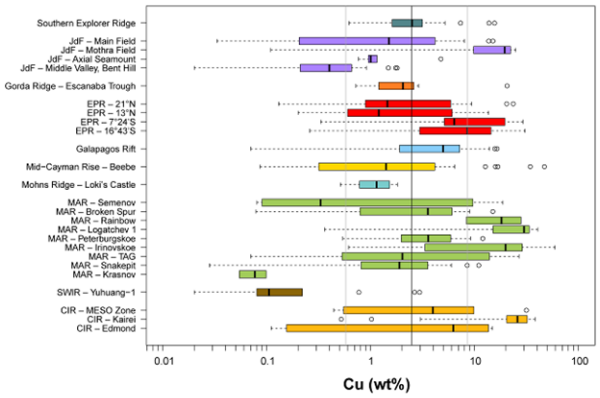
Southern Explorer Ridge
JdF – Main Field
JdF – Mothra Field
JdF – Axial Seamount
JdF – Middle Valley, Bent Hill
Gorda Ridge – Escanaba Trough
EPR – 21°N
EPR – 13°N
EPR – 7°24'S
EPR – 16°43'S
Galapagos Rift
Mid–Cayman Rise – Beebe
Mohns Ridge – Loki's Castle
MAR – Semenov
MAR – Broken Spur
MAR – Rainbow
MAR – Logatchev 1
MAR – Peterburgskoe
MAR – Irinovskoe
MAR – TAG
MAR – Snakepit
MAR – Krasnov
SWIR – Yuhuang–1
CIR – MESO Zone
CIR – Kairei
CIR – Edmond
0.01
0.1
1
10
100
Cu (wt%)

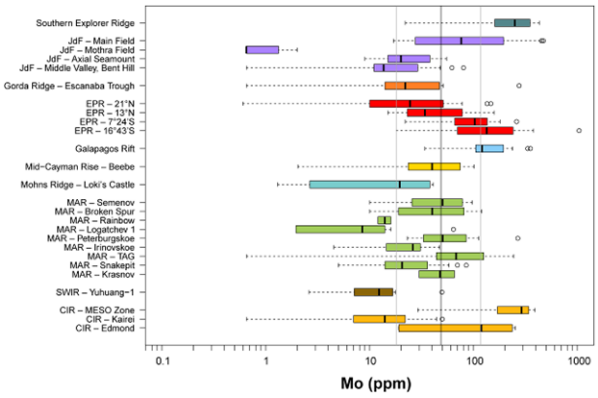
Southern Explorer Ridge
JdF – Main Field
JdF – Mothra Field
JdF – Axial Seamount
JdF – Middle Valley, Bent Hill
Gorda Ridge – Escanaba Trough
EPR – 21°N
EPR – 13°N
EPR – 7°24'S
EPR – 16°43'S
Galapagos Rift
Mid–Cayman Rise – Beebe
Mohns Ridge – Loki's Castle
MAR – Semenov
MAR – Broken Spur
MAR – Rainbow
MAR – Logatchev 1
MAR – Peterburgskoe
MAR – Irinovskoe
MAR – TAG
MAR – Snakepit
MAR – Krasnov
SWIR – Yuhuang–1
CIR – MESO Zone
CIR – Kairei
CIR – Edmond
0.1
1
10
100
1000
Mo (ppm)

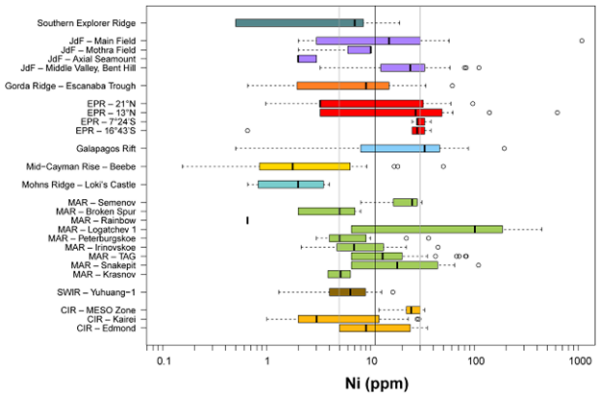
Southern Explorer Ridge
JdF – Main Field
JdF – Mothra Field
JdF – Axial Seamount
JdF – Middle Valley, Bent Hill
Gorda Ridge – Escanaba Trough
EPR – 21°N
EPR – 13°N
EPR – 7°24'S
EPR – 16°43'S
Galapagos Rift
Mid–Cayman Rise – Beebe
Mohns Ridge – Loki's Castle
MAR – Semenov
MAR – Broken Spur
MAR – Rainbow
MAR – Logatchev 1
MAR – Peterburgskoe
MAR – Irinovskoe
MAR – TAG
MAR – Snakepit
MAR – Krasnov
SWIR – Yuhuang–1
CIR – MESO Zone
CIR – Kairei
CIR – Edmond
0.1
1
10
100
1000
Ni (ppm)

1003

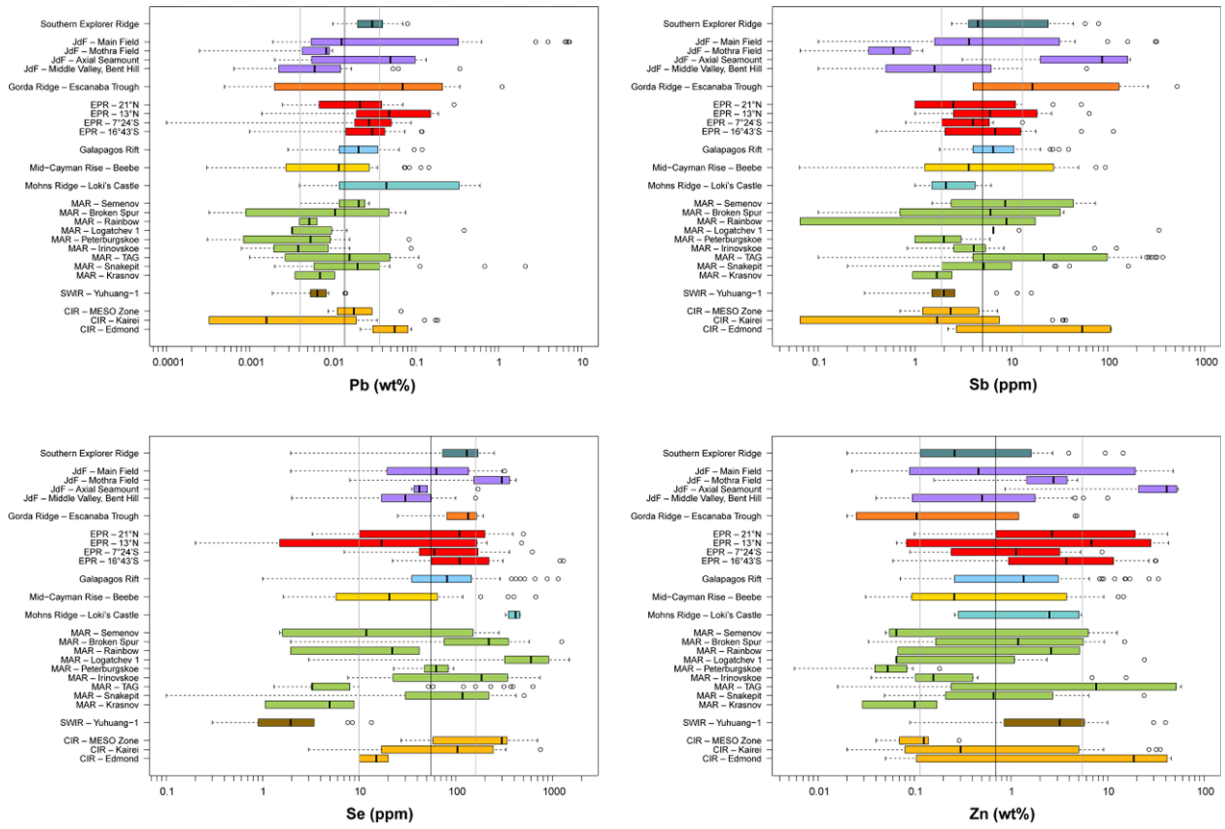

Figure 1. Box-and-whiskers plots indicating the distribution of elements in the various sites. The boxes comprise the data between the first and third quartile (Q1 and Q3). The thick bar inside the boxes is the median, while the whiskers are calculated as Q1-1.5×(Q3-Q1) and Q3+1.5×(Q3-Q1). The circles represent the outliers. The three vertical lines (from left to right) represent the Q1, median and Q3 of the global distribution of the specific element (see Table 2 for the values).

1011

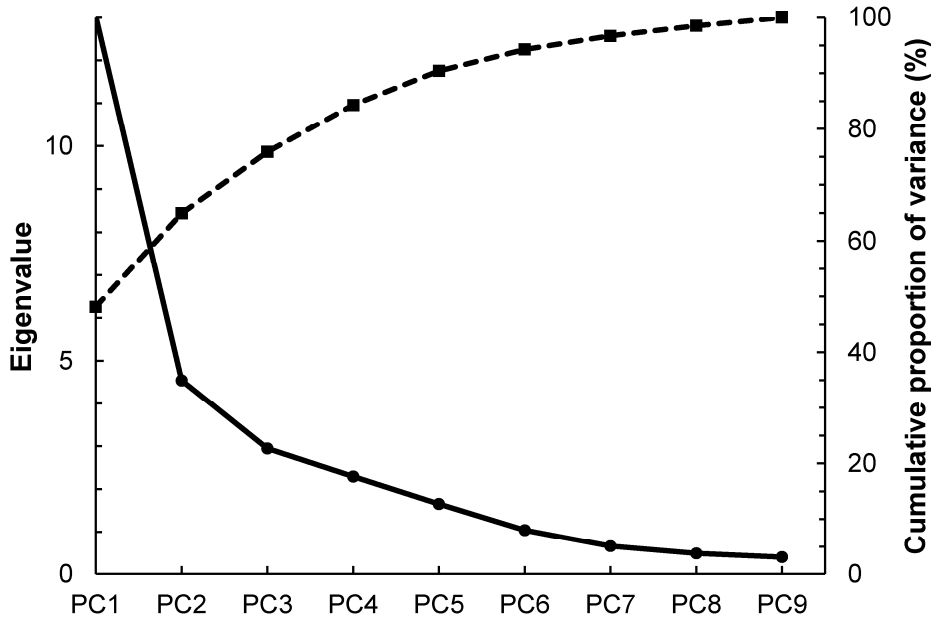

1012

1013 **Figure 2.** Screeplot resulting from the robust PCA. The first three components describe the

1014 greatest proportion of variance.

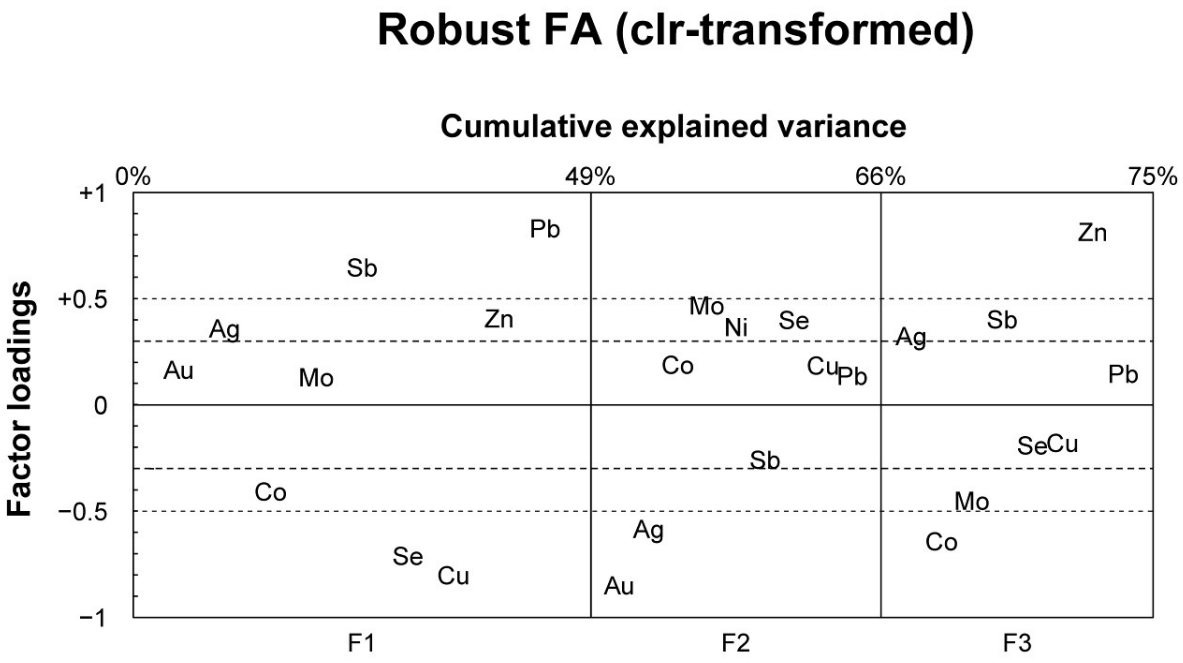

Figure 3. Factor loading plots for the clr-transformed MS data. The variables (elements) that most significantly affect the factors have loadings > 0.5 (thin dashed lines). Variables with loadings < 0.3 (thick dashed lines) are almost irrelevant and those with loadings < 0.1 are not reported in the plot.

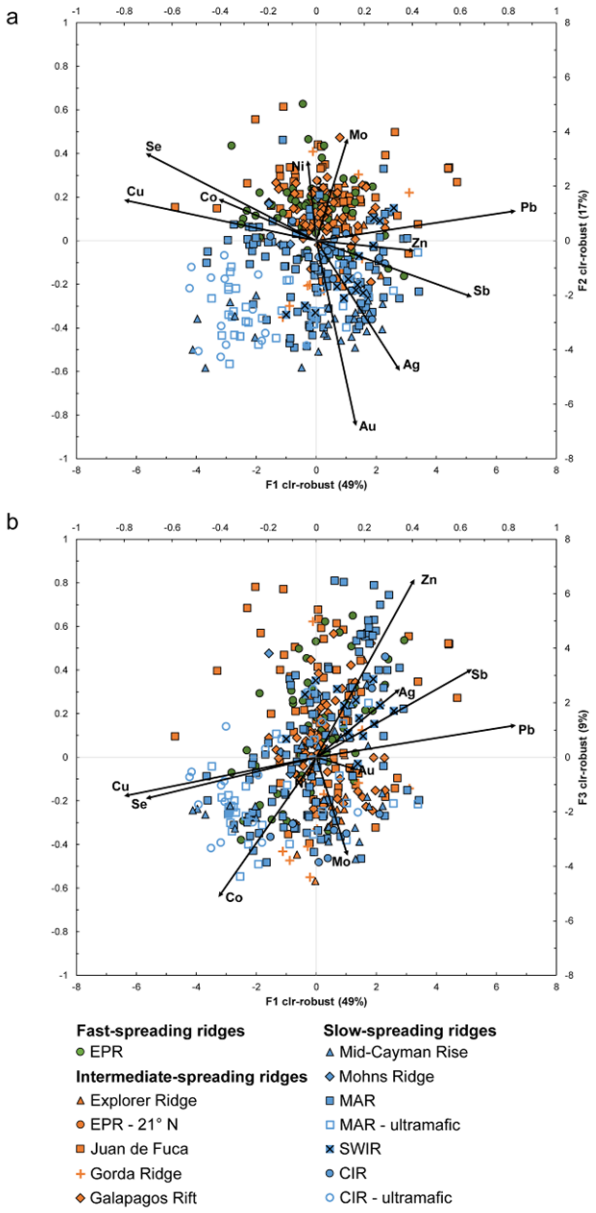

Figure 4. Biplots for the robust FA of clr-transformed MS data: a) F1 vs. F2; b) F1 vs. F3. Lower horizontal and right axes refer to the coordinates of the data points (scores), while upper

1024 horizontal and left axes refer to the coordinates of the variables (loadings). Data for individual
1025 sites are illustrated in Fig. S2.
1026

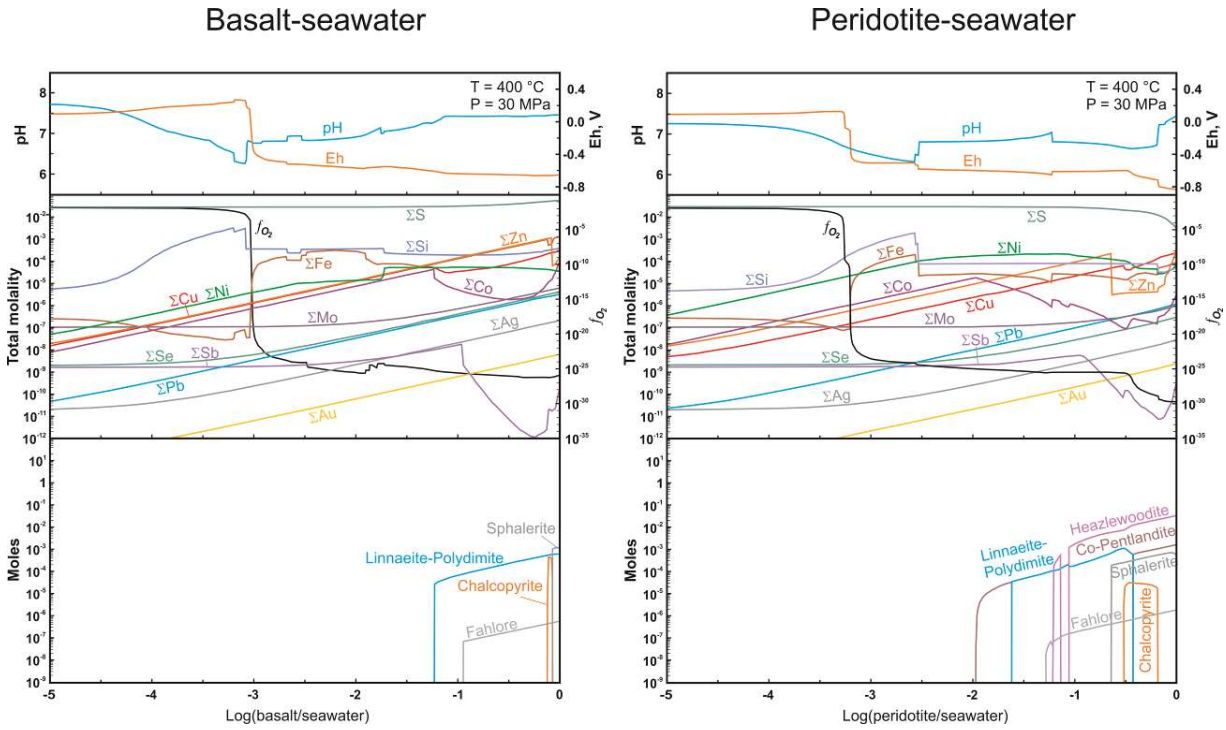

Figure 5. Physicochemical model of the interaction of seawater with basalt (left) and peridotite (right) at various r/w ratios (see Table SM2 for the compositions of the reactants). The geochemical characteristics (pH, Eh, concentration of selected dissolved elements and fO_2) of the hydrothermal fluid are reported in the upper and middle boxes. Only secondary sulfides developed in the matrix of altered rocks are shown here (bottom boxes), since they greatly affect the concentration of dissolved metals (see Fig. S5 and Fig. S6 for complete mineralogical data). Note that the slight increase of Mo, and Se in solution at high r/w ratios is probably an artifact, since the model does not allow for their isomorphic incorporation in alteration minerals.

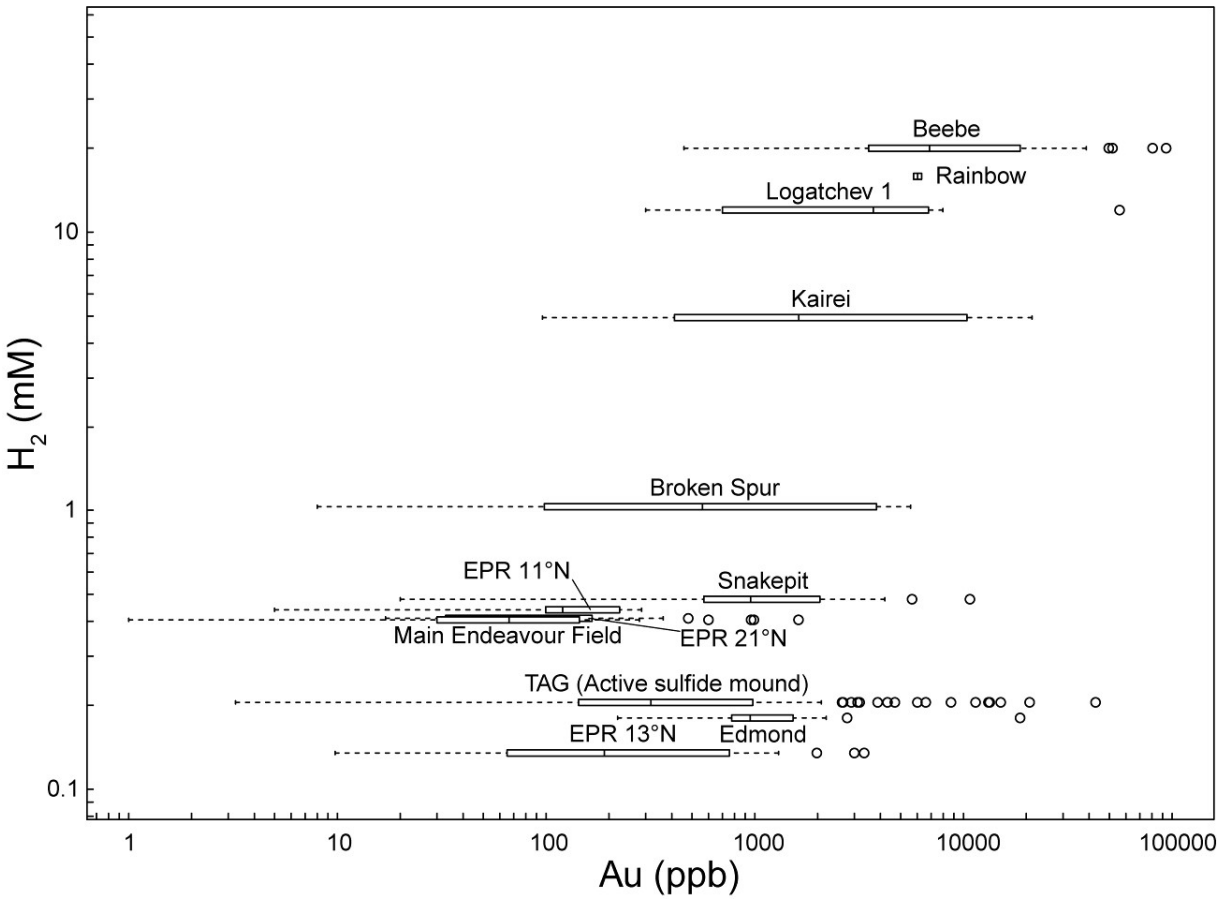

Figure 6. Distribution of Au concentration in SMS vs. H_2 in vent fluids. The meaning of the boxes and whiskers is the same as in Fig. 1. Data for vent fluids after Campbell et al. (1988), Charlou et al. (1996, 2002), Kumagai et al. (2008), Fouquet et al. (2010), Gallant and Von Damm (2006), Jean Baptiste et al. (1991), McDermott et al. (2018), Pester et al. (2011), Seewald et al. (2003), Seyfried et al. (2011), and Tivey (1995). Data for SMS are compiled in Table S1.

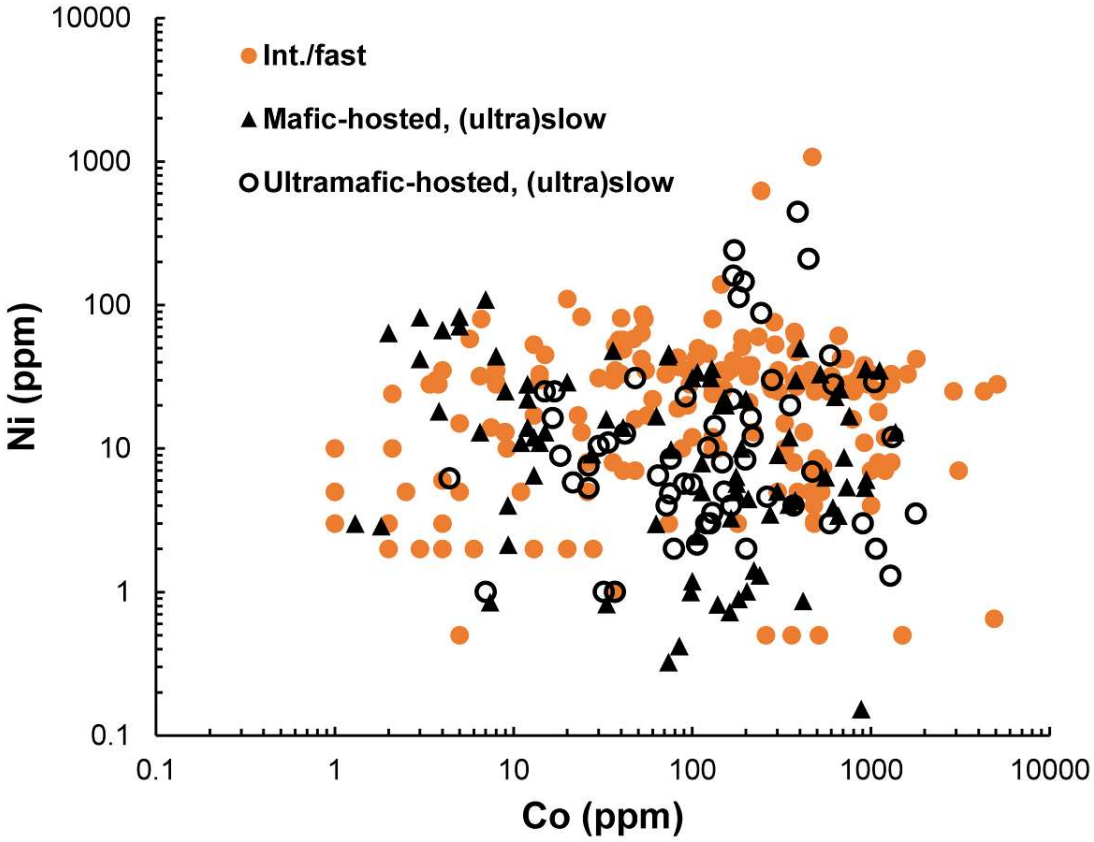

1044

1045 **Figure 7.** Cobalt vs. Ni concentrations in SMS from intermediate/fast-spreading ridges and slow-
1046 spreading ridges, distinguished between MORB- and ultramafic-hosted. Low-detects are not
1047 reported.

1048